Article

Cell Metabolism

Microbiota-derived acetate enables the metabolic fitness of the brain innate immune system during health and disease

Graphical abstract

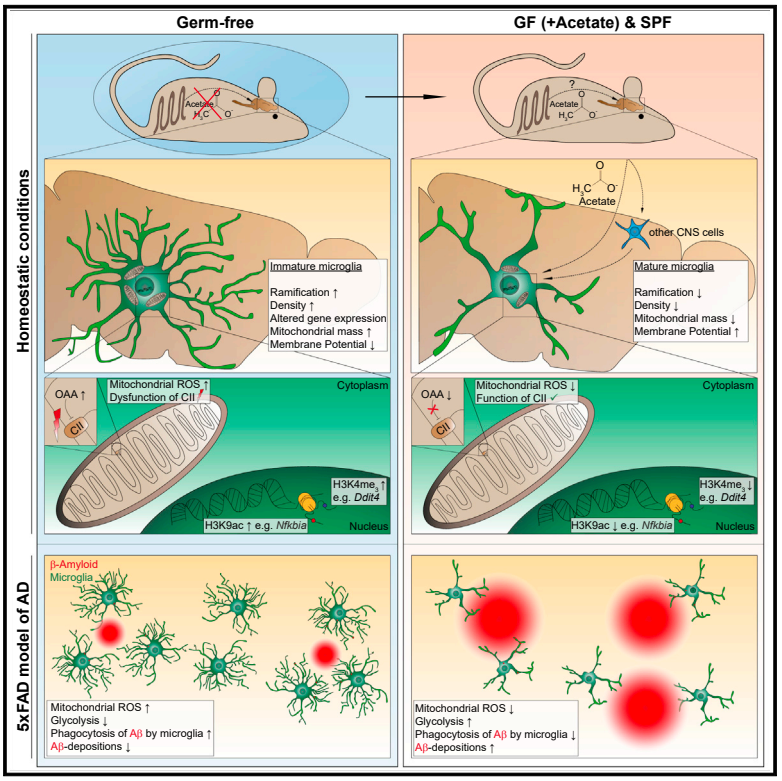

Highlights

- Altered metabolic features of microglia in the absence of host microbiota
- Bacteria-derived acetate modulates metabolic features of microglia during steady state
- Acetate regulates microglial functions during neurodegeneration

Authors

Daniel Erny, Nikolaos Dokalis, Charlotte Mezö, ..., Andrew J. Macpherson, Edward J. Pearce, Marco Prinz

Correspondence

marco.prinz@uniklinik-freiburg.de

In brief

Acetate is the critical microbiome-derived SCFA driving microglia maturation and regulating the homeostatic metabolic state. In addition, acetate modulates microglial phagocytosis of amyloid beta and disease progression in a mouse model for Alzheimer's disease.

Erny et al., 2021, Cell Metabolism *33*, 2260–2276
November 2, 2021
https://doi.org/10.1016/j.cmet.2021.10.010

CellPress

CellPress

Cell Metabolism

Article

Microbiota-derived acetate enables the metabolic fitness of the brain innate immune system during health and disease

Daniel Erny,[1,2,12] Nikolaos Dokalis,[1,3,12] Charlotte Mezö,[1,3,12] Angela Castoldi,[4] Omar Mossad,[1,3] Ori Staszewski,[1] Maximilian Frosch,[1] Matteo Villa,[4] Vidmante Fuchs,[1,3] Arun Mayer,[1] Jana Neuber,[1,3] Janika Sosat,[1,3] Stefan Tholen,[5] Oliver Schilling,[5] Andreas Vlachos,[6,9] Thomas Blank,[1] Mercedes Gomez de Agüero,[7] Andrew J. Macpherson,[7] Edward J. Pearce,[3,4,8,11] and Marco Prinz[1,9,10,13,*]

[1]Institute of Neuropathology, University of Freiburg, Freiburg, Germany
[2]Berta-Ottenstein-Programme, Faculty of Medicine, University of Freiburg, Freiburg, Germany
[3]Faculty of Biology, University of Freiburg, Freiburg, Germany
[4]Department of Immunometabolism, Max Planck Institute of Immunobiology and Epigenetics, Freiburg im Breisgau, Germany
[5]Institute of Surgical Pathology, Medical Center, University of Freiburg, Freiburg, Germany
[6]Department of Neuroanatomy, Institute of Anatomy and Cell Biology, Faculty of Medicine, University of Freiburg, Freiburg, Germany
[7]Maurice E. Müller Laboratories, Department for Biomedical Research (DBMR), University Clinic of Visceral Surgery and Medicine, Inselspital, University of Bern, Bern, Switzerland
[8]CIBSS - Centre for Integrative Biological Signalling Studies, University of Freiburg, Freiburg, Germany
[9]Center for Basics in NeuroModulation (NeuroModulBasics), Faculty of Medicine, University of Freiburg, Freiburg, Germany
[10]Signalling Research Centres BIOSS and CIBSS, University of Freiburg, Freiburg, Germany
[11]Present address: Bloomberg-Kimmel Institute for Cancer Immunotherapy, Johns Hopkins School of Medicine, Baltimore, MD 21287, USA
[12]These authors contributed equally
[13]Lead contact
*Correspondence: marco.prinz@uniklinik-freiburg.de
https://doi.org/10.1016/j.cmet.2021.10.010

SUMMARY

As tissue macrophages of the central nervous system (CNS), microglia constitute the pivotal immune cells of this organ. Microglial features are strongly dependent on environmental cues such as commensal microbiota. Gut bacteria are known to continuously modulate microglia maturation and function by the production of short-chain fatty acids (SCFAs). However, the precise mechanism of this crosstalk is unknown. Here we determined that the immature phenotype of microglia from germ-free (GF) mice is epigenetically imprinted by H3K4me3 and H3K9ac on metabolic genes associated with substantial functional alterations including increased mitochondrial mass and specific respiratory chain dysfunctions. We identified acetate as the essential microbiome-derived SCFA driving microglia maturation and regulating the homeostatic metabolic state, and further showed that it is able to modulate microglial phagocytosis and disease progression during neurodegeneration. These findings indicate that acetate is an essential bacteria-derived molecule driving metabolic pathways and functions of microglia during health and perturbation.

INTRODUCTION

Microglia are the main macrophage population in the central nervous system (CNS), critically involved in the pathogenesis of virtually all CNS disorders ranging from neuroinflammatory, neurodegenerative, and neurooncological diseases to neurodevelopmental psychiatric conditions (Colonna and Butovsky, 2017; Li and Barres, 2018; Prinz et al., 2019). Microglia are long-lived and exhibit plasticity in their responsiveness to diverse signals (Wendeln et al., 2018). They are recognized as vital regulators of CNS development and homeostasis by shaping other glial cells and neurons (Colonna and Butovsky, 2017; Hagemeyer et al., 2017).

Tissue-specific factors like colony-stimulating factor (CSF)1 and interleukin (IL)-34, as well as environmental factors, are known to govern microglial identity in the CNS (Amit et al., 2016; Erny et al., 2015; Gosselin et al., 2014; Lavin et al., 2014). Previously, we showed that gut bacteria maintain the maturation and function of microglia under steady-state conditions and following perturbations (Erny et al., 2015). For instance, mice housed under germ-free (GF) conditions, lacking all commensal bacteria, displayed an immature microglial phenotype with irregular cell numbers, changed morphology, and diminished antiviral functions (Erny et al., 2015; Erny and Prinz, 2020). We found that short-chain fatty acids (SCFAs), microbiota-derived bacterial fermentation products, were able to normalize the immature microglial phenotype (Erny et al., 2015). SCFAs have also been demonstrated to accelerate disease progression in a model of Parkinson's disease (PD)

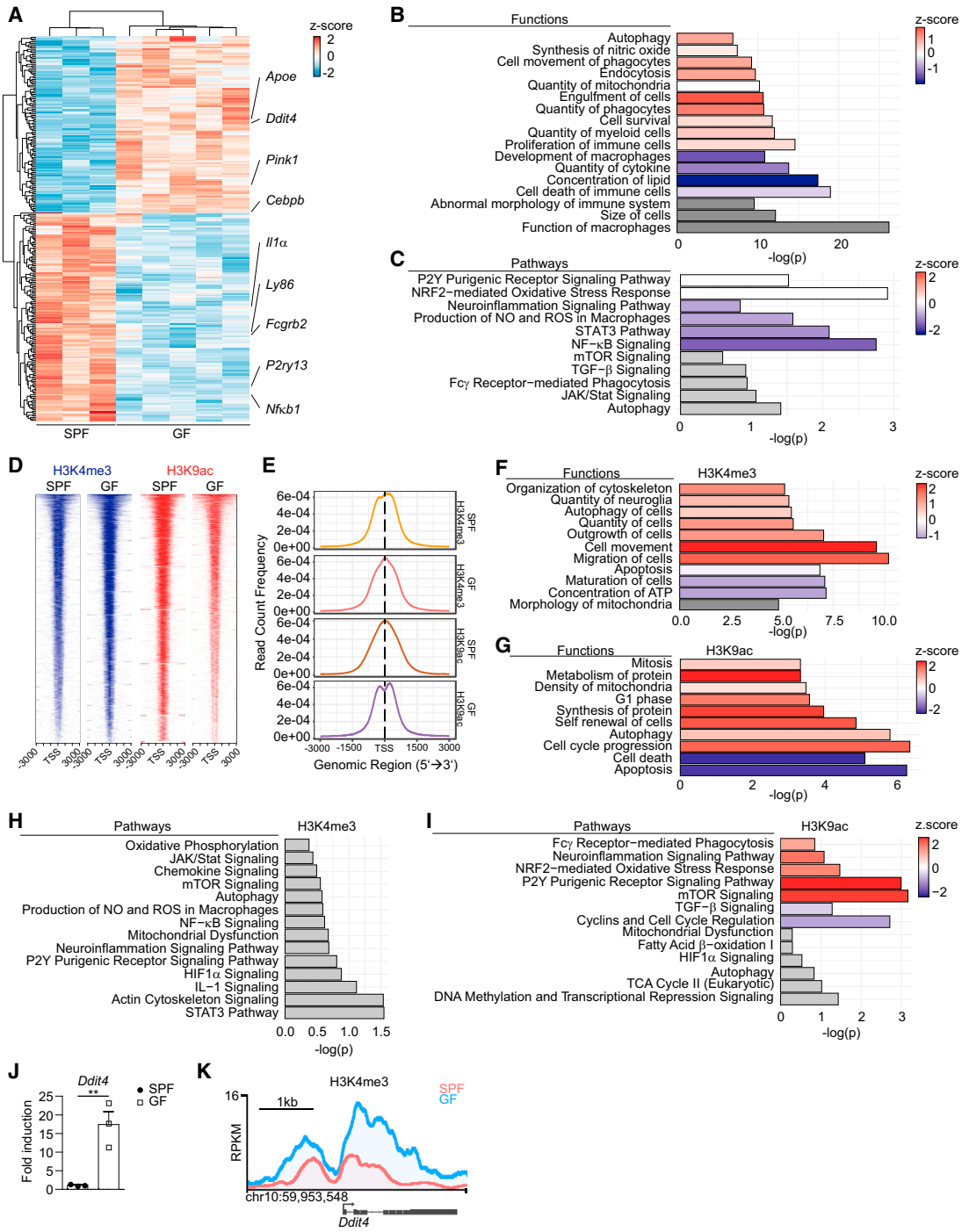

Figure 1. Absence of host microbiota alters genome-wide microglial methylation and acetylation profiles of metabolism-associated genes

(A) RNA-seq analysis presenting differentially expressed genes (DEGs) with an adjusted $p < 0.05$ in microglia from female SPF or GF animals. Color code presents *Z* score (red, upregulated; blue, downregulated). See also Table S1.

(B and C) Ingenuity pathway analysis (IPA) on DEGs in microglia from female SPF or GF mice based on an RNA-seq analysis. −log(p) and predicted activation *Z* scores (red, increased activity; blue, reduced activity; gray, no predicted *Z* score available) are shown. See also Tables S1 and S2.

(D) Distribution plots of H3K4me3 (left, blue) or H3K9ac (right, red) for microglia from SPF or GF mice within 3 kb centered on the transcription start side (TSS). One experiment with microglia from 4 individual SPF and GF female mice per group was performed. See also Tables S3, S4, S5, S6, and S7.

(E) Distribution plots of H3K4me3 (top) or H3K9ac (bottom) for microglia from female SPF or GF mice.

(F–I) IPA showing significantly changed functional (F and G) and canonical (H and I) pathways for genes with altered H3K4me3 or H3K9ac in their promoters in microglia of female GF animals compared to SPF controls. −log(p) and predicted activation *Z* scores (red, increased activity; blue, reduced activity; gray, no predicted *Z* score available) are shown. See also Tables S8 and S9.

(legend continued on next page)

(Sampson et al., 2016). In mouse models for Alzheimer's disease (AD), the absence of the host microbiota resulted in a reduction in amyloid beta (Aβ) burden (Harach et al., 2017; Mezö et al., 2020), suggesting that gut bacteria may worsen AD and PD by accelerating microglial exhaustion (Erny and Prinz, 2017). In contrast, during multiple sclerosis (MS), SCFAs, and in particular propionate, have been shown to have protective effects due to their ability to regulate mitochondrial function in circulating regulatory T cells (Haghikia et al., 2015), thereby improving regulatory function and modulating disease development (Duscha et al., 2020). The functional connection of the gut and CNS is conceptualized in the so-called gut-brain axis (Cryan et al., 2019).

In general, it is well established that many immune responses are accompanied by considerable changes in cellular metabolism (Caputa et al., 2019; O'Sullivan et al., 2019). For example, T cells utilize diverse metabolic pathways to enable differentiation and activation (Qiu et al., 2019). For microglia, however, most studies addressing cellular metabolism have utilized immortalized cell lines or primary microglia and bone marrow macrophage cultures *in vitro* (Borst et al., 2019; Ulland et al., 2017), with their attendant problems, and therefore insights about metabolic changes of microglia *in vivo* are scarce (Borst et al., 2019). Furthermore, the precise nature of the bacteria-derived products driving immunomodulation and the exact cellular pathways involved are unexplored.

We therefore sought to decipher which microglial functions are affected by host microbiota during homeostasis. We determined that altered expression of metabolic genes in microglia from GF mice is epigenetically imprinted. We subsequently profiled the metabolic state of *ex vivo* isolated microglia from GF mice and identified defined mitochondrial changes and associated dysfunctions leading to functional impairments of these cells. Further, we traced gut-derived acetate *in vivo* and detected an acetate-dependent adaption of the metabolic deficits in microglia from GF mice during steady state. We finally established that acetate had a modulating impact on the course of neurodegeneration through its ability to inhibit microglial phagocytosis.

RESULTS

Enhanced H3K4me3 and H3K9ac of metabolic microglial genes in the absence of commensal bacteria

To profile potential transcriptional changes in microglia from GF mice, we first performed bulk RNA sequencing (RNA-seq) (Figure 1A) and confirmed our previous findings (Erny et al., 2015). We observed substantial transcriptional changes with 256 up- and downregulated transcripts in microglia from GF mice compared to those from specific pathogen-free (SPF) controls (Table S1). Among the most differentially expressed genes (DEGs) were the proliferation-associated gene *DNA damage inducible transcript 4* (*Ddit4*, 4.04 $\log_2$ fold increased in microglia from GF mice compared to SPF) and the microglia activation gene *apolipoprotein E* (Sofer et al., 2005) (*Apoe*, 1.28 $\log_2$ fold increased in GF mice compared to SPF). In contrast, mRNA for *Il1a* and *Ly86* (encoding MD-1) were strongly diminished in GF microglia.

To obtain mechanistic insights into the microglial cellular functions and canonical pathways affected by microbiota deficiency, we performed ingenuity pathway analysis (IPA) (Figures 1B and 1C; Tables S2 and S3). Significant changes were apparent in the annotated functions "proliferation of immune cells" (up), "cell survival" (up), "development of macrophages" (down), and "quantity of cytokines" (down) or annotated pathways "STAT3 pathway" (down) or "neuroinflammation signaling pathway" (down), supporting the view that microglia in GF animals are immature. Notably, terms linked to metabolism such as reduced "concentration of lipid, quantity of mitochondria" and "ROS production in macrophages" were also different in GF microglia (Figures 1B and 1C).

It was previously described that the host microbiota affects open chromatin sides in microglia (Thion et al., 2018). To investigate whether the absence of host microbiota altered, in particular, histone methylation or acetylation of specific genes, we next performed genome-wide epigenetic profiling by chromatin immunoprecipitation sequencing (ChIP-seq) of H3K4me3 and H3K9ac, respectively (Figures 1D–1I). Although global levels of H3K4me3 revealed only subtle changes in microglia of GF mice compared to SPF controls, detailed analyses uncovered an elevated abundance of H3K4me3 at the proximal promoters of 239 genes (Tables S4 and S5). In contrast, increased levels of H3K9ac at the active promoters of 613 genes were found in microglia from GF mice (Tables S6 and S7).

We next classified the genes with altered H3K4me3 and H3K9ac levels according to their molecular functions (Figures 1F and 1G; Table S8) and canonical pathways (Figures 1H and 1I; Table S9) by IPA. Similar categories to those apparent in the RNA-seq analysis were also represented in the ChIP-seq analysis, including "reduced maturation of cells and increased quantity of cells" for H3K4me3 and "increased cell cycle progression" and "density of mitochondria" for H3K9ac (Figures 1B, 1C, and 1F–1I). Notably, expression of *Ddit4*, revealed by RNA-seq to be increased in microglia from GF mice (Figure 1A), a result confirmed by qRT-PCR (Figure 1J), also had a greater abundance of H3K4me3 in its proximal promoter in GF microglia versus SPF microglia associated with transcriptional activation (Figure 1K). Additionally, proteome analysis revealed similar functional and canonical pathway categories of isolated microglia from SPF and GF mice (Figure S1; Tables S10 and S11).

Together, these data indicate that a life-long absence of host microbiota causes changes in gene expression and associated epigenetic changes in histone acetylation and methylation marks at defined promoter regions of genes that control not only microglial proliferation, morphology, and activation but also metabolic functions, including mitochondrial density.

(J) *Ddit4* mRNA measured by qRT-PCR in microglia from SPF and GF mice (mixed sex). Gene expression was normalized to *β-Actin*. Data are representative of three independent experiments.

(K) ChIP-seq data showing the coverage of H3K4me3 in the promoter region for *Ddit4* from microglia of female SPF and GF mice. RPKM values are shown on the y axis. Average of 4 individual samples from one experiment are shown.

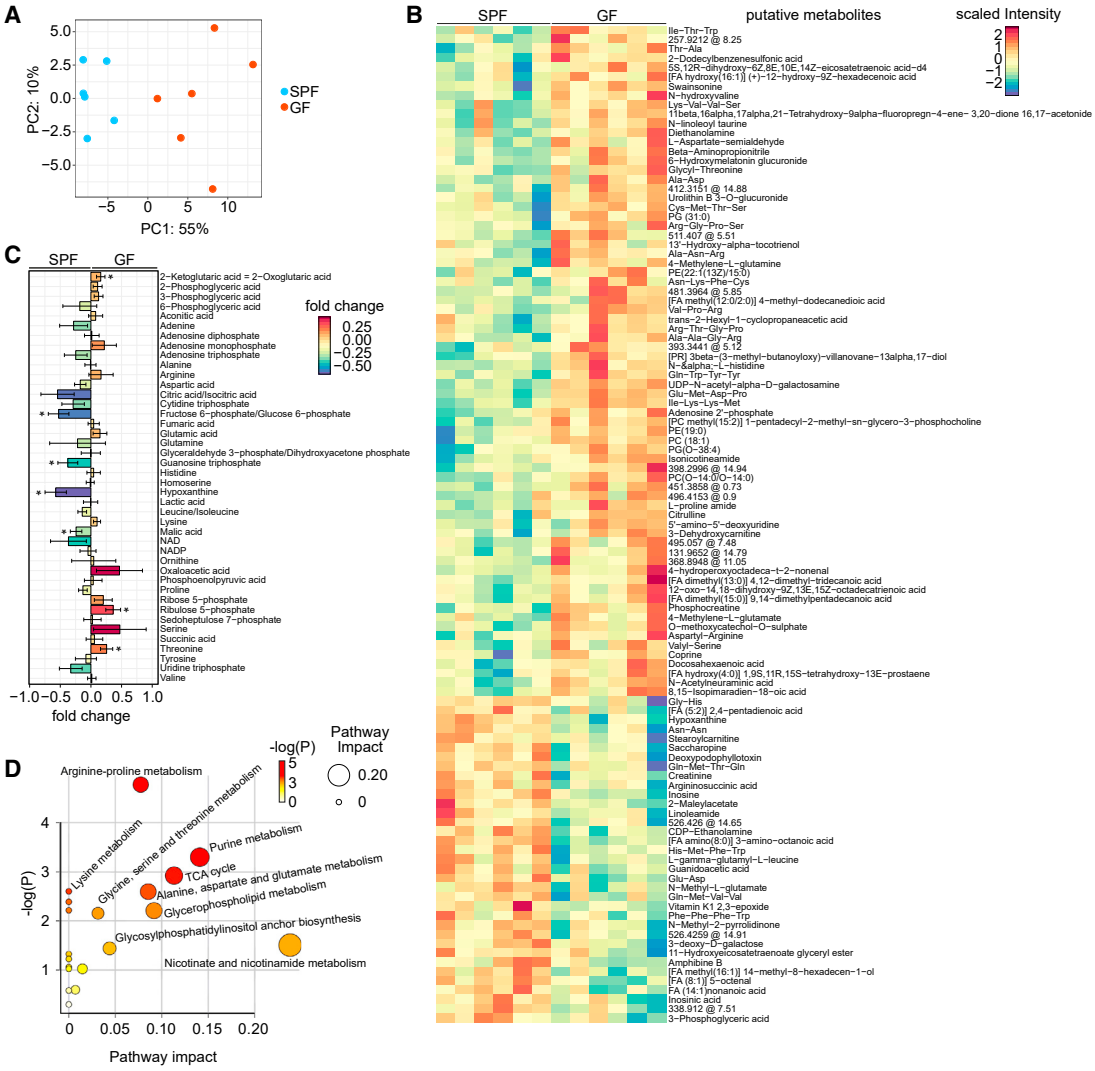

Figure 2. Lack of commensal microbes changes microglia metabolic signature

(A) Principal component analysis (PCA) plot of the PC 1 and 2 of significantly altered metabolites from six SPF and six GF microglia samples. One experiment with female mice was performed.

(B) Heatmap of significantly altered metabolites from non-targeted metabolite profiling between the SPF (left) and GF (right) group. Color scale indicates scaled intensity: intensities > 0 are upregulated (red); intensities < 0 are downregulated (blue). See also Table S12 and Figure S2.

(C) Fold change plot of detected metabolites from non-targeted metabolite profiling of SPF and GF microglia. Color scale indicates the degree of $\log_2$ fold change (red, upregulated >0.5; violet, downregulated <−0.5). See also Table S13 and Figure S3.

(D) Pathway matches of significantly changed metabolites in GF microglia compared to SPF microglia based on targeted and non-targeted metabolite profiling. Circle size reflects the pathway impact and color code visualizes −log(p) value (white = 0, yellow = 1, orange = 2, red > 3).

Changed microglial metabolic profiles in the absence of host microbiota

We next focused on the possibility that mitochondrial metabolic functions might be affected by host microbiota. We performed a comprehensive metabolite profiling of *ex vivo* fluorescence-activated cell sorting (FACS)-isolated microglia from SPF and GF mice and detected in total 759 metabolites (Table S12). Valid sum formulas matching known annotations could be calculated for 597 of these, whereas 162 were classified as unknown (Table S12). Statistical analysis determined 107 putative metabolites, which were significantly different ($p < 0.05$) between SPF and GF microglia and principal component analysis (PCA) of these revealed a clear separation between both groups (Figure 2A). Among these metabolites, 72 showed increased and 35 decreased abundance in microglia from GF mice compared to SPF microglia (Figures 2B and S2). Generally, we noticed several changes in amino acids and peptides indicating abnormal amino acid metabolism. Alterations in citrulline, phosphocreatine, argininosuccinic, and guanidoacedic acid levels indicated perturbations in arginine and proline metabolism. Moreover, altered levels of inosine, inosinic acid, and hypoxanthine pointed to perturbed purine metabolism in microglia from GF mice. Numerous lipids and fatty acids, such as [FA-amino(8:0)] 3-amino-octanoic acid, were depleted in microglia from GF mice compared to SPF microglia.

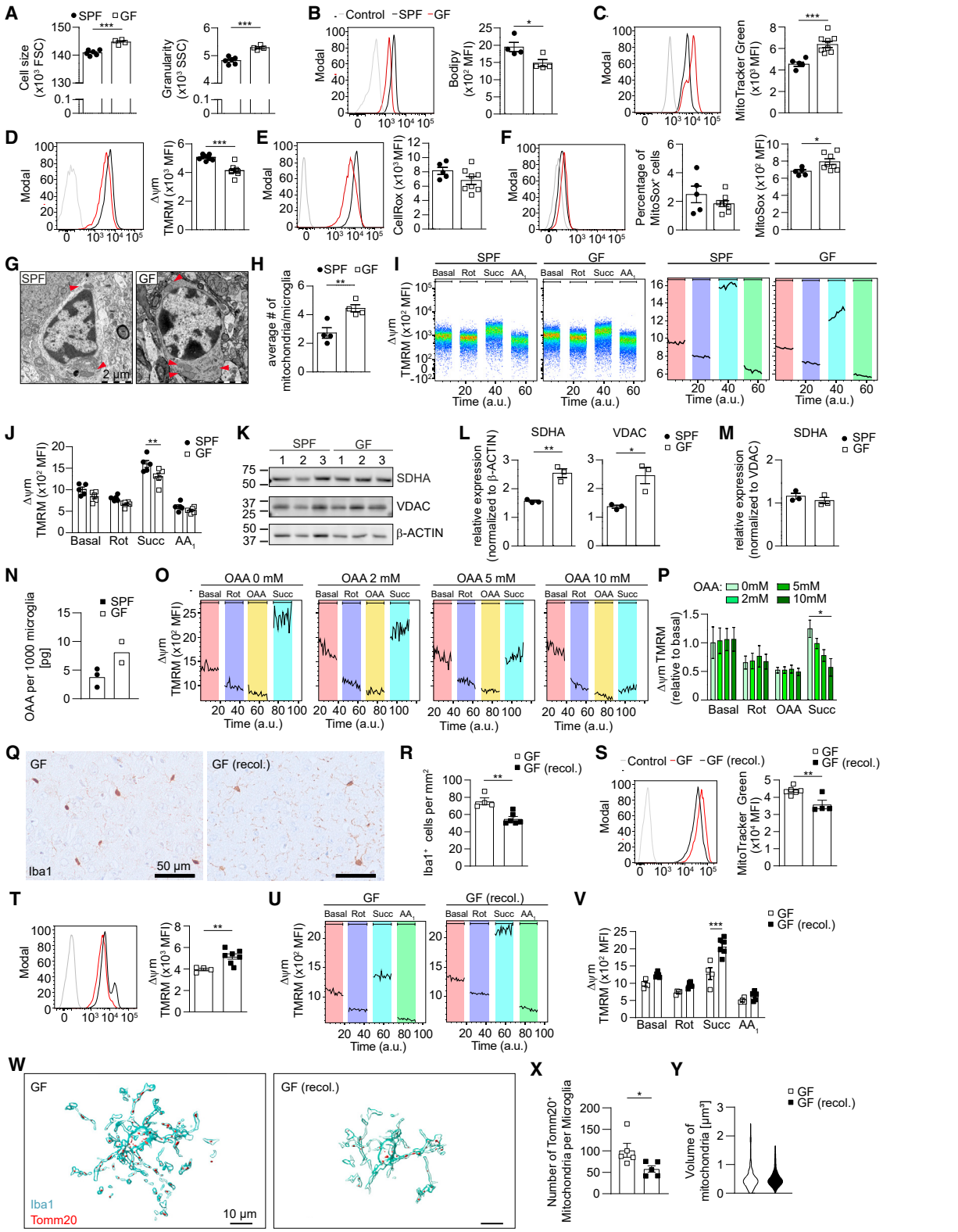

Figure 3. Diminished mitochondrial functions in microglia from GF mice

(A–F) Representative cytometry graphs demonstrating (A) microglial cell size (FSC, forward scatter, left) and granularity (side scatter, SSC, right), (B) lipids (Bodipy), (C) mitochondrial mass (MitoTracker Green), (D) mitochondrial membrane potential Δψm (tetramethylrhodamine methyl ester, TMRM), (E) total ROS (CellRox), and (F) mitochondrial ROS (MitoSox) on CD11b^{+}CD45^{low} microglia from male GF (red lines) and SFP mice (black lines) and respective controls (gray

(legend continued on next page)

To explore central metabolic pathways in microglia in more detail, we then carried out a targeted analysis of 62 metabolites, of which 42 were measurable in microglial cells derived from SPF and GF mice (Figures 2C and S3; Table S13). Seven metabolites differed significantly between SPF and GF microglia. One of these was ribulose 5-phosphate, which was increased in GF microglia, suggesting increased purine metabolism and enhanced nucleotide production, which broadly correlates with previously described elevations in microglial density and proliferation in GF mice (Erny et al., 2015; Thion et al., 2018). Furthermore, metabolites from the tricarboxylic acid (TCA) cycle such as 2-ketoglutaric acid (up) and malic acid (down) were found to be significantly affected in GF microglia while citrate showed a trend toward being less abundant. Oxaloacetate (OAA) accumulated by tendency in microglia from GF mice whereas GF microglia showed tendentially reduced levels of adenosine triphosphate (ATP).

Taken together, these data indicate that elements of the TCA cycle and purine metabolism, as well as additional metabolic pathways in microglia, are affected by the presence of the host microbiota (Figure 2D).

Host microbiota control functionality of complex II of the respiratory chain during homeostasis

Our data indicated that mitochondrial metabolism is disturbed in microglia from GF mice. To address this in greater detail, we next performed a comprehensive functional analysis of this cell compartment. First, we used extracellular flux analysis to perform a mitochondrial stress test on microglia isolated *ex vivo* from SPF and GF mice. Surprisingly, we observed only minor differences in oxygen consumption rates between the cells (Figures S4A–S4C). Noticeably, neither microglia from SPF nor GF mice possessed any spare respiratory capacity (SRC) (Figures S4B and S4C). This was confirmed by a comparison with peritoneal macrophages, whereby only 1.5×10^5 plated peritoneal macrophages had a significantly higher basal and maximal respiration and SRC compared to 3×10^5 microglia (Figures S4A and S4D), indicating that *ex vivo* isolated microglia present a relatively low metabolic turnover compared to other macrophages in this experimental setting and that the Seahorse approach might not be sensitive enough for assessing metabolic features of *ex vivo* isolated microglia. In addition, we investigated extracellular acidification rates (ECARs), a measure of the production of lactate due to glycolysis, which were similar between microglia from SPF and GF mice (Figures S4E and S4F), as was the uptake of glucose (Figure S4G), while ECAR measurements of microglia showed comparable levels to peritoneal macrophages (Figures S4E and S4H).

Subsequently, we applied flow cytometry-based approaches with higher sensitivity. First, we observed larger and more granular Dump$^-$CD11b$^+$CD45^{low} microglia from GF mice compared to those from SPF mice (Figures 3A and S4A). Elevated intracellular granularity can be due to increases in the abundance of organelles such as lysosomes, lipid droplets, and mitochondria. However, we observed reduced lipids, as measured by Bodipy, in GF microglia (Figure 3B), which was consistent with the observed changes in several fatty acids revealed by metabolite profiling (Figure 2B). Moreover, measurement of LysoTracker staining and CD68 expression revealed that GF status had no effect on the lysosomal compartment (Figures S4I and S4J). However, microglia from GF mice had significantly increased mitochondrial content, as measured by MitoTracker Green staining (Figure 3C). These mitochondria differed from SPF microglia in that they had reduced mitochondrial membrane potential ($\Delta\psi$m), as measured by tetramethylrhodamine methyl ester (TMRM) staining (Figure 3D). We also noted that the amount of total cellular reactive oxygen species (ROS) (CellRox) (Figure 3E) and the percentage of microglia positive for mitochondrial ROS (MitoSox) (Figure 3F) were largely similar in microglia from GF and SPF mice. GF microglia produced significantly more mitochondrial ROS compared to SPF controls (Figure 3F). Taken together, these observed changes in mitochondrial mass,

lines). In addition, quantifications of the mean fluorescence intensities (MFIs) and percentages of MitoSox$^+$ cells and are depicted. Data are representative of three independent experiments.

(G and H) Transmission electron microscopy (TEM) images of microglia (G) in the cortex of adult SPF and GF male mice harboring mitochondria (red arrowheads) in the cytoplasm and quantification thereof (H).

(I) Oxidative phosphorylation measured by flow cytometry over time (arbitrary units, a.u.). Representative cytometry graphs of the $\Delta\psi$m, which was manipulated by rotenone (Rot), succinate (Succ), and antimycin A_1 (AA_1) on microglia from male SPF (left) and GF mice (right). Data are representative of three independent experiments.

(J) Quantification of the $\Delta\psi$m. Data are representative of three independent experiments.

(K–M) Representative immunoblots for mitochondrial succinate dehydrogenase (SDHA) and voltage-dependent anion-selective channel (VDAC) derived from *ex vivo* isolated microglia from male GF and SFP mice are shown (K). Quantification is normalized to (L) β-ACTIN or (M) VDAC. Data are representative of two independent experiments.

(N) Quantification of oxaloacetic acid (OAA) in FACS-isolated microglia. Microglia from six brains were pooled to one sample.

(O and P) Inhibition of complex II by OAA was analyzed from microglia from male SPF mice by flow cytometry. (O) Representative cytometry graphs of the $\Delta\psi$m and (P) normalized quantification thereof (n = 3). Data are representative of two independent experiments.

(Q) Representative Iba1$^+$ immunohistochemistry in cortex of GF male mice and recol. GF mice.

(R) Quantification thereof. Scale bar, 50 μm. Data are representative of two independent experiments.

(S and T) Representative cytometry graphs demonstrating (S) microglial mitochondrial mass and (T) $\Delta\psi$m on microglia from male GF (red lines) and recol. GF mice (black lines) and respective controls (gray lines). In addition, quantifications of the MFIs are depicted. Data are representative of two independent experiments.

(U) Oxidative phosphorylation measured by flow cytometry over time (arbitrary units, a.u.). Representative cytometry graphs of the $\Delta\psi$m on microglia from male GF mice (left) and recol. GF mice (right).

(V) Quantification thereof. Data are representative of two independent experiments.

(W) Imaris-based 3D reconstruction of representative Iba1$^+$ cortical microglia and Tomm20$^+$ mitochondria of GF and recol. GF male mice. Scale bars, 10 μm.

(X and Y) Quantification thereof.

See also Figures S4 and S5.

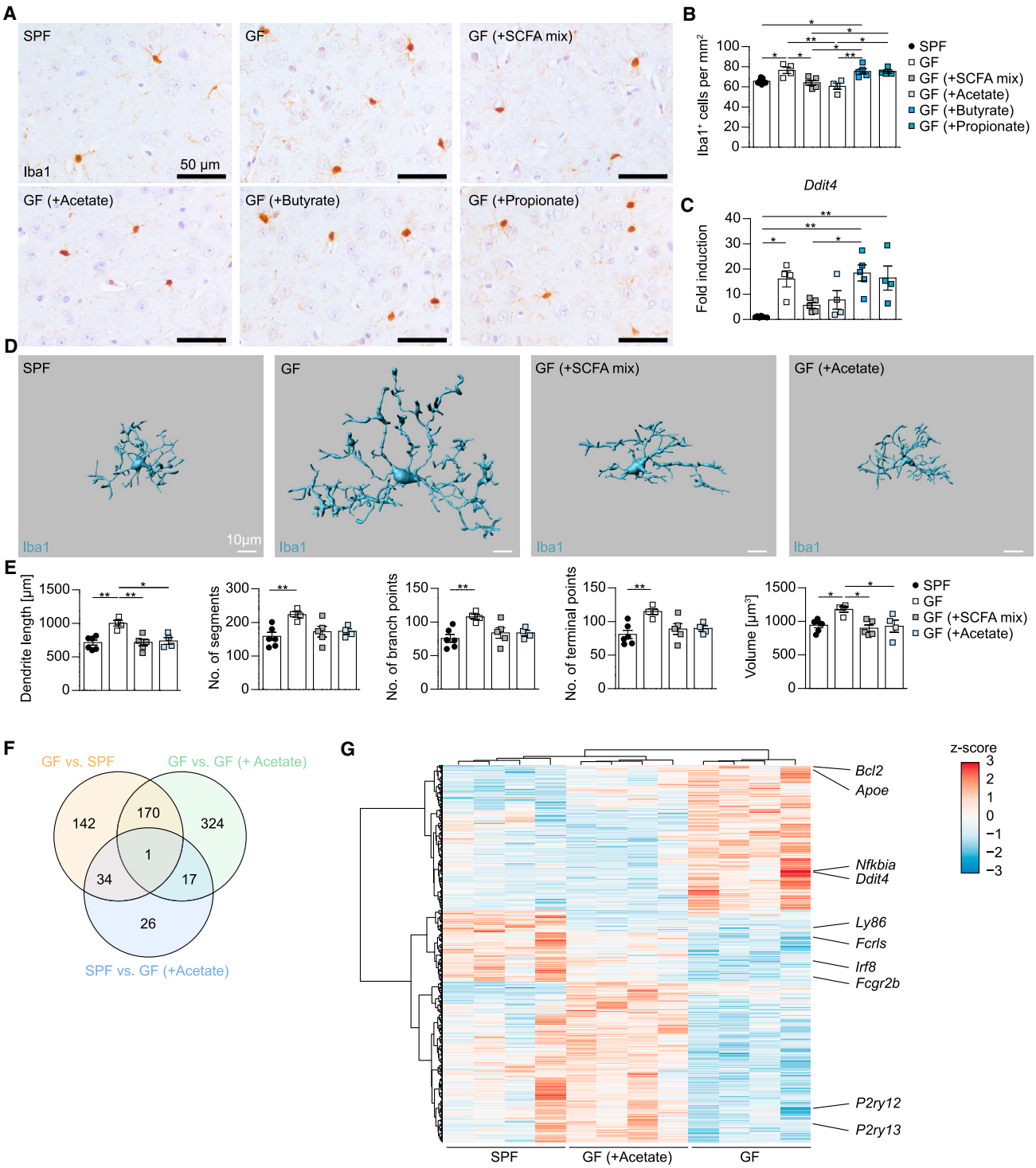

Figure 4. Microbiota-derived acetate restores microglial properties of GF microglia

(A) Representative Iba1$^+$ immunohistochemistry in cortex of SPF, GF, or GF male mice treated with SCFA mixture or acetate, butyrate, or propionate alone.

(B) Quantification thereof. Scale bar, 50 µm. Data are representative of three independent experiments.

(C) *Ddit4* mRNA measured by qPCR. Gene expression was normalized to *β-Actin*. Data are representative of three independent experiments.

(D) Imaris-based 3D reconstruction of representative Iba1$^+$ cortical microglia of GF male mice treated or untreated with SCFA mixture or acetate alone. Scale bars, 10 µm.

(E) Quantification thereof.

(legend continued on next page)

$\Delta\psi$m, and mitochondrial ROS supported the view that mitochondrial biology was significantly affected in GF microglia.

We subsequently quantified the number of microglial mitochondria by transmission electron microscopy (TEM) (Figure 3G). Ultrastructurally, microglia exhibited typical morphological features such as distinctive heterochromatin patterns, small cytoplasmic margins, and immunoreactivity for Iba1 and PU.1 (Figure S4K). In accordance with the increased mitochondrial mass measured using MitoTracker and flow cytometry, TEM revealed increased numbers of mitochondria in GF microglia (Figures 3G and 3H).

We next refocused on understanding the differences in $\Delta\psi$m in more detail. We measured $\Delta\psi$m directly by TMRM staining over time before complex I (C1) was inhibited by rotenone, which caused the $\Delta\psi$m to decline equivalently in microglia from SPF and GF mice (Figures 3I and 3J). Adding the CII substrate succinate allowed the inhibition of CI to be bypassed, restoring activity of the electron transport chain (ETC) and re-establishment of $\Delta\psi$m (Figures 3I and 3J). The succinate-driven increase in $\Delta\psi$m was clearly impaired in microglia from GF mice (Figures 3I and 3J). As expected, inhibition of the CIII by antimycin A_1 (AA_1) collapsed $\Delta\psi$m in both populations of microglia (Figures 3I and 3J). The experimental setup used in the flow cytometry-based evaluation was verified independently for *ex vivo* isolated microglia and peritoneal macrophages by Seahorse analysis (Figure S4L). We found that $\Delta\psi$m increased equivalently in SPF and GF microglia in response to pyruvate and malate, which fuel CI, indicating that microglial CI function is unaffected by microbiota (Figure S4M). Additionally, we supplied CIV with ascorbate and tetramethyl phenylenediamine and did not detect any alterations (data not shown), pointing to a selective CII impairment in microglia from GF animals. This was unlikely to be due to differences in expression of CII components, since SDHA (a major component of CII) was expressed equivalently in microglia from GF and SPF mice (Figures 3K–3M).

An alternative explanation for reduced CII activity was that microglia from GF mice had increased levels of endogenous CII inhibitors. Among these, OAA (Schollmeyer and Klingenberg, 1961) was found to be increased (Figures 3N and 2C). We found that OAA, in a dose-dependent fashion, was able to inhibit succinate-induced CII activity in SPF microglia (Figures 3O and 3P), supporting the possibility that OAA could suppress CII activity in microglia from GF mice.

Next, we investigated whether postnatal recolonization of GF mice was sufficient to modulate microglial properties. GF mice were therefore exposed to SPF donor mice after birth and examined 8 weeks later. Recolonized GF mice displayed significantly less microglia compared to GF controls (Figures 3Q and 3R). Furthermore, mitochondrial mass and $\Delta\psi$m were restored upon recolonization (Figures 3S and 3T), resulting in a sufficiently increased $\Delta\psi$m after addition of succinate as compared to microglia from GF mice (Figures 3U and 3V). Detailed Imaris-based 3D reconstruction revealed a decreased microglial volume of recolonized GF mice compared to GF mice (Figures 3W, S5A, and S5B). Notably, microglia showed fewer Tomm20$^+$ mitochondria in recolonized GF mice compared to GF mice, whereas the mitochondrial volumes remained unchanged, excluding a role for altered mitochondrial fusion or fission (Figures 3W–3Y). Furthermore, we depleted gut bacteria postnatally by antibiotic (ABX) treatment and found reduced $\Delta\psi$m after succinate application in microglia from ABX-treated mice compared to SPF controls (Figures S5C and S5D), highlighting a dynamic and plastic interplay of gut bacteria and microglial metabolic features.

Together, these data revealed significant alterations in the composition of the mitochondrial network and defective CII activity in microglia from GF mice under homeostatic conditions.

Bacteria-derived acetate restores diminished microglia fitness during steady state

The SCFAs acetate, propionate, and butyrate are bacterial fermentation products that we and others have recently shown to be essential for microglia maturation and function during homeostasis and infection (Erny et al., 2015; Sampson et al., 2016). However, it has remained unclear whether the different SCFAs act on microglia only synergistically or also individually. We therefore provided a mixture of SCFAs, or acetate, propionate, or butyrate individually, to GF mice for 4 weeks via their drinking water. As expected based on prior work, a mixture of SCFAs was able to reduce heightened microglia densities found in GF to normal microglia numbers observed under SPF conditions (Figures 4A and 4B). This effect was recapitulated by acetate alone, but not by butyrate or propionate. The correction of microglia numbers by acetate supplementation was accompanied by reduced expression of *Ddit4*, whereas butyrate and propionate had no effect on *Ddit4* mRNA levels (Figure 4C). Detailed analysis of microglia cell morphology revealed that only mixed SCFAs or acetate reversed defects in microglia proportions (Figures 4D and 4E). Microglial F4/80 levels were not modulated by these treatments (Figure S5E).

To examine the effect of acetate on microglial transcriptomic profile, we isolated microglia from SPF, GF, and acetate-treated GF mice and analyzed genome-wide mRNA expression profiles by RNA-seq (Figures 4F and 4G). In general, 856 genes were modulated under these conditions (Figure 4F; Table S14). Notably, microglia from SPF and GF (+acetate) displayed only 26 unique DEGs while microglia from SPF and GF mice as well as microglia from GF and GF (+acetate) mice showed 142 and 324 unique DEGs, respectively (Figures 4F and 4G; Table S14). Among the DEGs, we observed in GF microglia upregulated expression of *Apoe* and *Ddit4*. *P2ry12* showed a reduced expression in microglia from GF mice that was restored in the presence of acetate (Figure 4G). Subsequent IPA of DEGs revealed, e.g., restored NFkB signaling and immune response of cells (Tables S15 and S16).

We then asked whether mitochondrial metabolic deficits could be rectified by SCFAs. We found that a mixture of SCFAs, and acetate alone, normalized mitochondrial numbers in microglia from GF mice (Figures 5A, 5B, and S5F). Examination of the

(F) Venn diagram depicting the different regulated and overlapping genes between FACS-isolated microglia of male SPF, GF, and GF (+acetate) mice.
(G) RNA-seq analysis presenting DEGs with an adjusted $p < 0.05$ in microglia of male SPF, GF, and GF (+acetate) mice. Color code presents *Z* score (red, upregulated; blue, downregulated).
See also Tables S14, S15, and S16 and Figure S5.

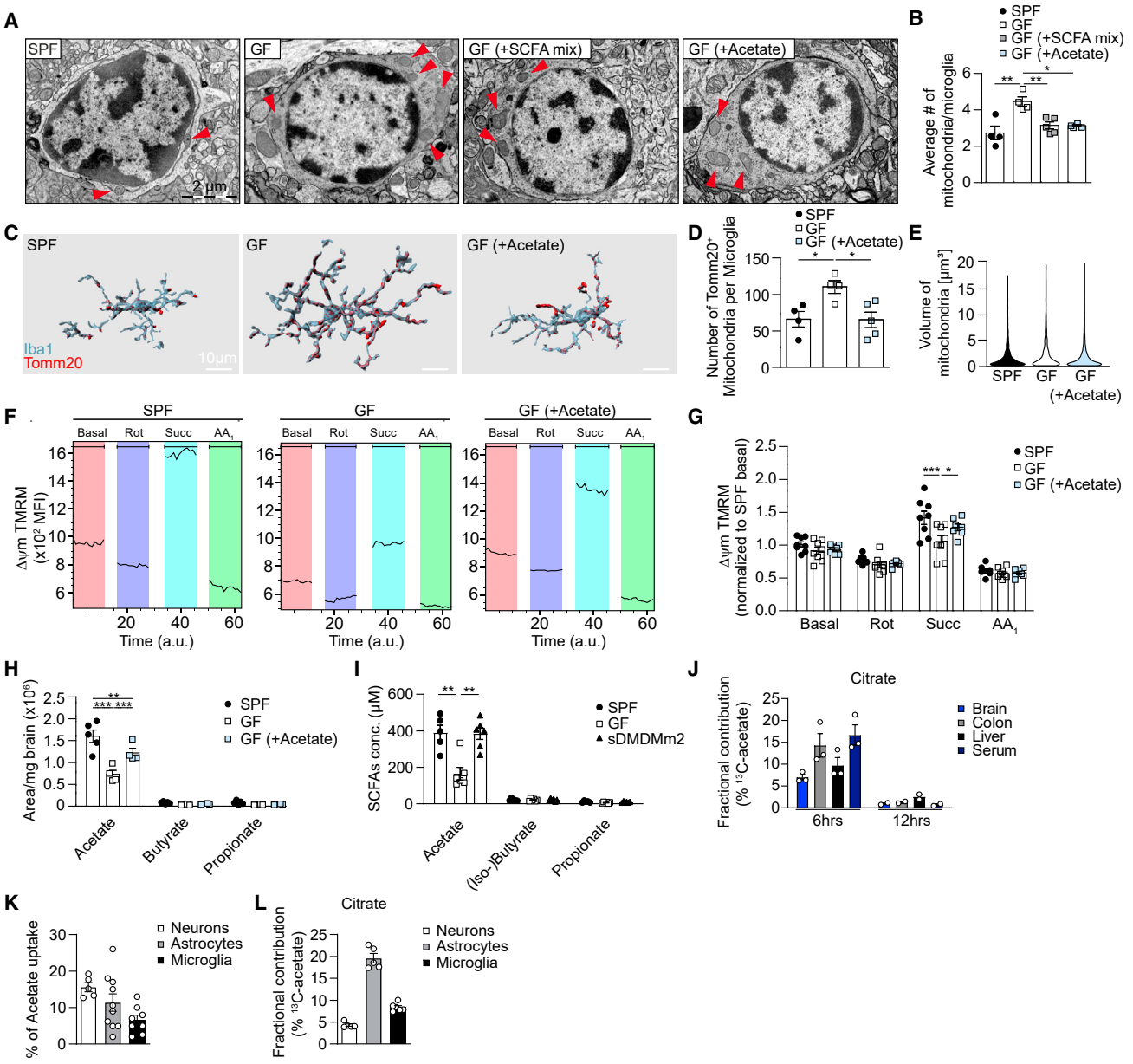

Figure 5. Microbiota-derived acetate restores metabolic insufficiency of GF microglia

(A) Representative TEM images of cortical microglial cells. Red arrowheads display mitochondria in the cytoplasm.

(B) Quantification thereof.

(C) Imaris-based 3D reconstruction of representative Iba1^{+} cortical microglia and Tomm20^{+} mitochondria.

(D and E) Quantification thereof. Scale bars, 10 µm.

(F) Measurement of oxidative phosphorylation by flow cytometry over time. Representative cytometry graphs of the Δψm from microglia from male SPF (left) and GF mice (middle) and acetate-treated GF mice (right).

(G) Quantification thereof. Data are pooled from three independent experiments.

(H) Abundance of acetate, butyrate, and propionate in brains of male SPF and GF mice treated orally or untreated for 4 weeks with acetate.

(I) Concentration of acetate, (iso-)butyrate, and propionate in the serum of male SPF, GF, and sDMDMm2 mice.

(J) Fraction of acetate-derived ^{13}C-labeled carbons for citrate in the brain, colon, liver, and serum of male GF mice after 6 and 12 h of oral application. Data are representative of two independent experiments.

(K) Percentage of acetate uptake from the media in cultured primary neurons, astrocytes, and microglia after 6 h incubation time with 5 mM acetate. Data are representative of two independent experiments.

(L) Fraction of acetate-derived ^{13}C-labeled carbons for citrate in primary neurons, astrocytes, and microglia after 6 h incubation time. Data are typical of two independent experiments.

See also Figures S5 and S6.

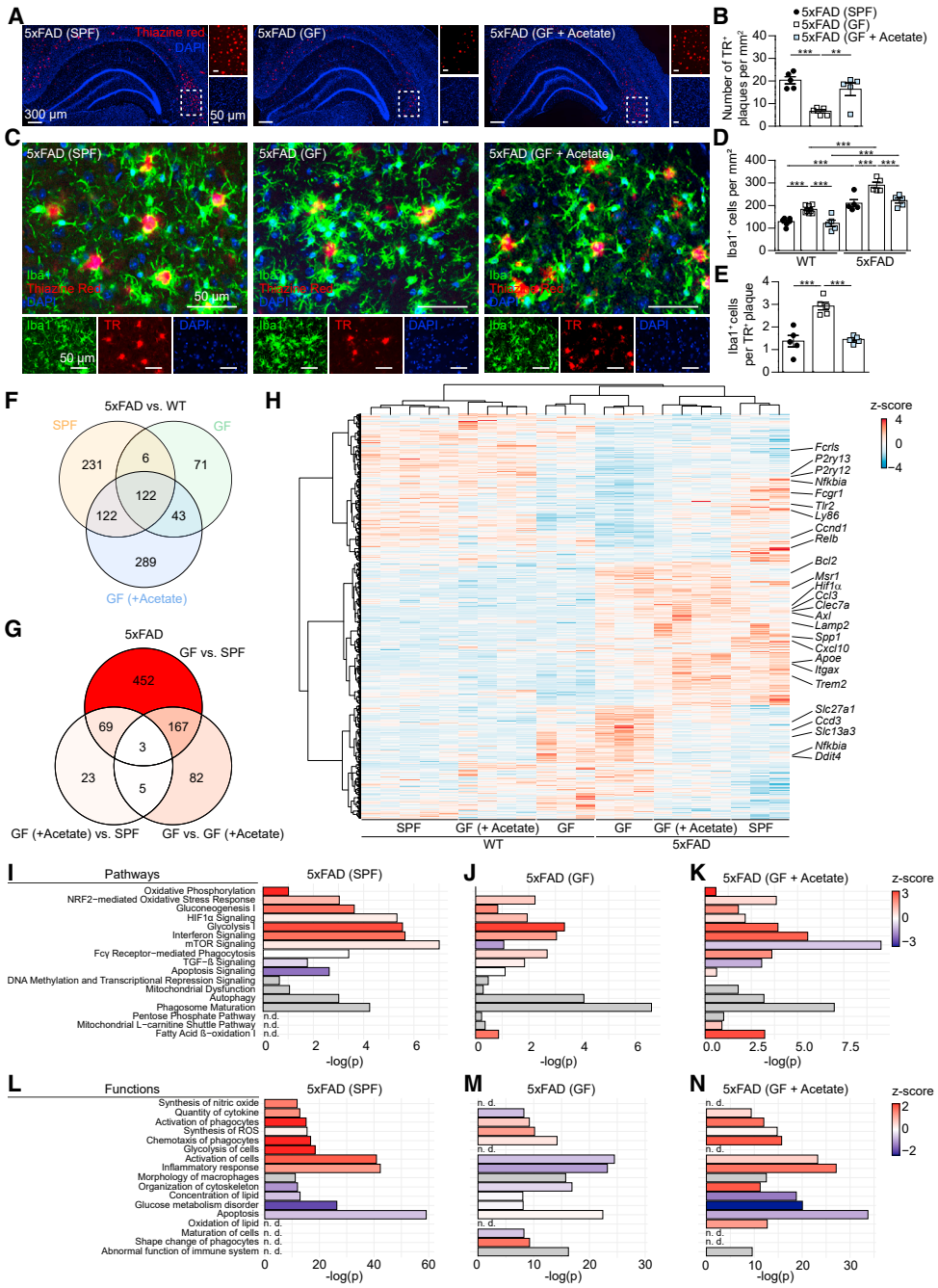

Figure 6. Acetate increases hippocampal Aβ depositions of 5xFAD mice

(A) Representative immunofluorescence images of thiazine red (TR; red) in 16-week-old male SPF, GF, and GF 5xFAD mice treated orally with acetate for 8 weeks. Nuclei were stained with 4,6-diamidino-2-phenylindole (DAPI; blue). Scale bars, 300 μm (overview) and 50 μm (insert).

(B) Quantification of the number of TR^+ Aβ plaques per area (mm^2).

(C) Representative immunofluorescence images of TR (red) and Iba1 (green) on sections containing hippocampus tissue. Nuclei were stained with DAPI (blue). Scale bar, 50 μm.

(D and E) Quantification of $Iba1^+$ parenchymal (D) and TR^+ plaque-associated (E) microglia.

(F and G) Venn diagrams depicting the different regulated and overlapping genes (F) between FACS-isolated hippocampal microglia of male 5xFAD animals compared to respective non-transgenic littermates of the same conditions, SPF, GF, or GF (+acetate), and (G) between 5xFAD animals.

(H) RNA-seq analysis presenting DEGs with an adjusted $p < 0.05$ in hippocampal microglia of male SPF, GF, and GF (+acetate) 5xFAD and WT animals. Color code presents *Z* score (red, upregulated; blue, downregulated). See also Table S17.

(legend continued on next page)

spatial dimensions of Tomm20^{+} mitochondria in microglia by 3D reconstruction confirmed that there were more mitochondria per microglia from GF mice compared to SPF mice, but revealed unaltered mitochondrial volumes and sphericities (Figures 5C–5E and S5G–S5J). Most importantly, we found that acetate supplementation of GF mice was sufficient to restore the $\Delta\psi$m in microglia after addition of succinate (Figures 5F and 5G). These findings indicate that CII-associated microglial dysfunction can be rescued by acetate treatment.

Our data indicated that acetate from the gut is able to affect the biology of CNS cells. Consistent with this, mass spectrometry allowed detection of acetate in the CNS of mice from all experimental groups, albeit at significantly lower levels in GF compared to SPF mice. CNS acetate levels in GF mice were significantly increased as a result of 4 weeks of oral acetate treatment (Figure 5H). Detected levels of butyrate and propionate in the CNS from differently housed mice were negligible. In order to demonstrate that the presence of gut bacteria is augmenting SCFA levels, we quantitatively measured SCFA concentrations in the serum of sDMDMm2 mice that harbor a stable defined moderately diverse mouse microbiota consisting of 12 selected acetate-producing bacterial stains (Uchimura et al., 2016). sDMDMm2 mice showed comparable acetate levels in the serum as SPF controls, whereas GF mice showed significantly reduced abundance of acetate (Figure 5I). To specifically trace gut-derived acetate *in vivo*, we provided ^{13}C-acetate by oral gavage to GF mice and 6 and 12 h later measured the incorporation of ^{13}C-labeled carbon in brain, colon, liver, and serum (Figures 5J and S6A). Significant incorporation of acetate-derived ^{13}C was measured in several metabolites of the TCA cycle in all tested organs and serum at 6 h post-treatment. To examine whether CNS cells can absorb acetate directly, primary cells were exposed to acetate *in vitro* (Figure 5K). Neurons, astrocytes, and microglia all acquired acetate from the medium (Figure 5K) and incorporated acetate-derived ^{13}C into various metabolites including the TCA cycle intermediates citrate, alpha-ketoglutarate, fumarate, malate, and succinate (Figures 5L and S6B), highlighting direct uptake and use of acetate by microglia. Collectively, our data revealed that microglia attributes and metabolic functions are controlled by gut-derived acetate.

Acetate alone modulates microglial functions during neurodegeneration

Microglia are believed to contribute to the pathogenesis of AD—the most prevalent neurodegenerative disease (Datta et al., 2018; Mildner et al., 2011; Prinz et al., 2011; Sarlus and Heneka, 2017). We previously identified that commensal bacteria impair AD pathology in the 5xFAD mouse model (Mezö et al., 2020), although whether or not bacteria-derived products such as SCFAs modulate Aβ burden is unknown (Mossad and Erny, 2020). To examine whether gut bacteria shape microglial immune responses by permissive chromatin marks involved in the gene regulation of distinct cytokines and metabolic genes, we employed 16-week-old male 5xFAD mice. Analysis of microglia from SPF and GF 5xFAD mice revealed higher levels of H3K9ac at or around the transcriptional start sites of proinflammatory genes such as *Cxcl10* and *Isg15*. Metabolic-related genes such as *Pgk1* (phosphoglycerate kinase 1) involved in the first ATP-generating step of the glycolytic pathway showed increased H3K9ac in microglia from SPF 5xFAD mice compared to microglia form GF 5xFAD mice (Figure S6C), suggesting higher expression and metabolic activity of SPF microglia in 5xFAD mice. As expected (Mezö et al., 2020), GF 5xFAD mice displayed diminished Aβ deposition and smaller plaque size, as visualized by thiazine red (TR), in hippocampus when compared to SPF 5xFAD mice (Figures 6A, 6B, and S7A–S7C). Notably, administration of acetate through drinking water for 8 weeks to GF 5xFAD mice prior to analysis resulted in increased numbers of larger TR^{+} Aβ plaques, comparable to those from SPF 5xFAD mice (Figures 6A, 6B, and S7A–S7C). The diminished plaque load in GF 5xFAD mice was accompanied by an increased density of Iba1^{+} parenchymal microglia (Figures 6C and 6D). An evaluation of TR^{+} plaque-associated Iba1^{+} microglia (those cells less than 10 μm from the TR^{+} plaques) revealed significantly more cells in close proximity to Aβ in GF 5xFAD mice than in SPF 5xFAD mice, and acetate treatment reversed this effect (Figure 6E).

To investigate the effect of acetate on microglia in more detail, hippocampal microglia from SPF, GF, and acetate-treated GF mice were analyzed by RNA-seq (Figures 6F–6H). Notably, microglia from SPF and GF (+acetate) 5xFAD mice displayed 481 and 576 DEGs compared to WT controls, respectively, while microglia from GF 5xFAD mice showed only 242 DEGs compared to non-transgenic animals (Figures 6F and 6H; Table S17). Comparing solely microglia from 5xFAD mice, we detected 452 unique DEGs in microglia of the GF and SPF group, while microglia from GF and GF (+acetate) showed 82 unique DEG and microglia from GF (+acetate) and SPF 5xFAD mice presented 23 unique DEGs (Figure 6G). Among the DEGs, we observed increased expression of genes attributed to Aβ stimulation, such as *Clec7a*, *Axl*, *Apoe*, *Itgax*, or *Trem2* (Figure 6H). Subsequent IPA revealed, e.g., upregulated interferon signaling in all three groups, although to a lesser degree in microglia from GF 5xFAD mice compared to wild-type (WT) animals (activation *Z* scores: SPF 5xFAD versus WT, 2.309; GF 5xFAD versus WT, 1.667; GF [+acetate] 5xFAD versus WT, 2.496) (Figures 6I–6K; Table S18). As a response to the diseased CNS, microglia from all three groups showed upregulated glycolysis and gluconeogenesis pathways whereby the significance was considerably decreased in microglia from GF 5xFAD mice (Figures 6I–6K; Table S18). Interestingly, TGF-β signaling was found to be upregulated only in microglia from GF 5xFAD mice, and in contrast, the functional annotations "quantity of cytokine," "activation of cells," "inflammatory response," and "chemotaxis of phagocytes" were down in the GF 5xFAD group and restored by acetate supplementation (Figures 6I–6N; Tables S18 and S19). In contrast, IPA predicted upregulated synthesis "of ROS" in microglia from GF 5xFAD mice (Figures 6L–6N; Table S19).

(I–N) Diagrams depict (I–K) canonical pathway and (L–N) functional results of IPA on DEGs in hippocampal microglia of male SPF, GF, and GF (+ acetate) 5xFAD animals compared to WT littermates of the same housing/treatment conditions. Diagram depicts −log(p) values and predicted activation *Z* scores (red, increased activity; blue, reduced activity; gray, no predicted *Z* score available; N.d., not detectable). See also Tables S18 and S19.
See also Figures S6 and S7.

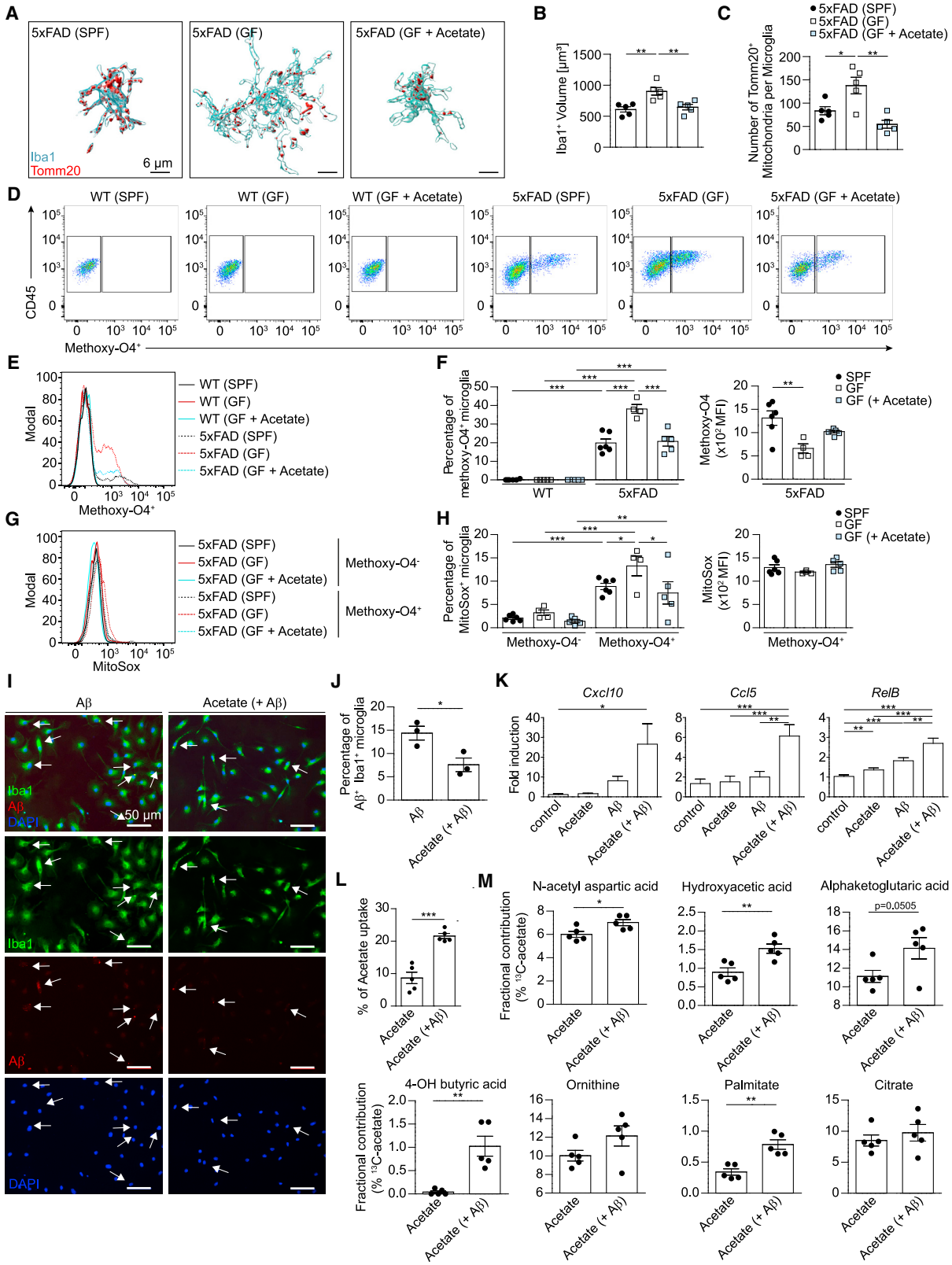

Figure 7. Acetate modulates microglia function during neurodegeneration

(A) Imaris-based 3D reconstruction of representative Iba1$^+$ TR$^+$ plaque-associated microglia and Tomm20$^+$ mitochondria. Scale bars, 6 μm.
(B and C) Quantification thereof.

(legend continued on next page)

As described above, microglia from GF mice displayed defects in CII function under steady-state conditions (Figures 3I and 3J). In contrast, Aβ-engulfing microglia, as indicated with methoxy-O4 (MXO4) incorporation, displayed no differences in the elevated Δψm upon succinate application (Figure S7D), indicating that CII seems not to be influenced by gut bacteria in the 5xFAD model. In addition, we analyzed the glucose uptake in $MXO4^-$ and $MXO4^+$ microglia from SPF and GF 5xFAD mice (Figure S7E). In line with the RNA-seq data (Figures 6I–6K; Table S18) and ChIP data (Figure S6C), we found reduced glucose uptake in microglia from GF 5xFAD mice, further supporting impaired glycolysis (Figure S7E).

Next, we analyzed the morphology of TR^+ plaque-associated microglia from SPF, GF, and acetate-treated GF 5xFAD mice (Figures 7A, 7B, and S7F). Notably, microglia from GF 5xFAD mice were more ramified compared to microglia from SPF and GF (+acetate) 5xFAD mice. Further, we observed higher numbers of $Tomm20^+$ mitochondria in plaque-associated microglia from GF 5xFAD mice compared to SPF 5xFAD mice (Figures 7A and 7C). Supplementation of acetate to GF 5xFAD mice restored both microglial morphology and the number of mitochondria in plaque-associated microglia (Figures 7A–7C and S7G), while the average and percentile mitochondrial volume and sphericity remained unaffected (Figures S7H–S7J).

It has been proposed that plaque-associated microglia are critical in restricting senile plaque formation in AD by improved migration and increased phagocytosis compared to non-pathology-linked microglia (Keren-Shaul et al., 2017; Meyer-Luehmann and Prinz, 2015). We thus investigated whether microglial uptake of Aβ is influenced by acetate. We observed higher percentages of $MXO4^+$ microglia under GF conditions (Figures 7D–7F) as described recently (Mezö et al., 2020). Notably, supplementation of acetate restored the percentage of $MXO4^+$ microglia to SPF levels (Figures 7D–7F), indicating that microglial phagocytosis of Aβ is modified by acetate.

To check whether acetate is also able to shape microglial metabolism during neurodegeneration, we analyzed microglial mitochondrial ROS production. Interestingly, the percentage of $MitoSox^+$ $MXO4^+$ microglia from 5xFAD mice was elevated, and this was significantly further enhanced if the cells were from GF 5xFAD mice (Figures 7G and 7H). Acetate treatment of GF 5xFAD mice normalized the percentage of $MXO4^+$ $MitoSox^+$ microglia to levels seen in microglia from SPF 5xFAD mice (Figures 7G and 7H), which is in accordance with the RNA-seq data whereby we observed activation of the synthesis of ROS pathway (Figures 6L and 6M; Table S19). $MXO4^+$ microglia exhibited increased Δψm and CellRox signals compared to $MXO4^-$ microglia, but these parameters showed only subtle modulation by acetate (Figures S7K and S7L).

To examine whether microglial acetate uptake is altered by the presence of Aβ, primary microglia were exposed to Aβ with and without acetate *in vitro* (Figure 7I). Previous reports have shown impaired Aβ uptake of microglia by increased proinflammatory cytokine expression (Babcock et al., 2015; Koenigsknecht-Talboo and Landreth, 2005). In line, the percentage of $Iba1^+$ $Aβ^+$ microglia was significantly decreased in the presence of acetate (Figure 7J), and the gene expression of *Cxcl10*, *Ccl5*, and *Relb* was upregulated when acetate and Aβ were applied together (Figure 7K). Notably, microglia acquired more acetate from the medium in the presence of Aβ (Figure 7L) and incorporated slightly more acetate-derived ^{13}C into various metabolites including TCA cycle intermediates (Figures 7M and S7M), suggesting that acetate fuels at least partially the TCA cycle.

In sum, these data indicate that gut-derived acetate modulates microglial functions in the 5xFAD mouse model for AD.

DISCUSSION

Here, we describe novel aspects of the gut-brain interplay, namely that the SCFA acetate modulates physiological microglial functions and is additionally able to modify AD pathology by shaping microglial innate immune mechanisms. We further identify host microbiota as an essential inducer of microglial mitochondrial functions. We found that the absence of gut microbiota led under homeostasis to a defined functional impairment of CII of the ETC, which correlated with other perturbations in mitochondrial function. These mitochondrial deficiencies were rectified by acetate, which the cells were able to use to fuel the TCA cycle.

It is recognized that host commensals are necessary for maintaining microglial maturation and function in the healthy and diseased CNS (Erny et al., 2015; Erny and Prinz, 2017; Sampson

(D) Gating of methoxy-$O4^+$ (MXO4) microglia from male SPF, GF, and acetate-treated GF 5xFAD mice and age-matched WT controls. Characteristic dot plots are shown.
(E) Representative cytometric graph of $MXO4^+$ microglia from male SPF (black line), GF (red line), and acetate-treated GF (blue line) WT mice and SPF (dashed black line), GF (dashed red line), and acetate-treated GF (dashed blue line) 5xFAD mice.
(F) Quantifications of the MFI and percentages of $MXO4^+$ microglia cells are depicted. Data are representative of two independent experiments.
(G) Typical cytometric graphs of the microglial mitochondrial ROS.
(H) Quantifications of the MFI and percentages of MitoSox positively labeled cells and are depicted. Data are representative of two independent experiments.
(I) Representative immunofluorescence images of cultured $Iba1^+$ primary microglia (green) after monomeric amyloid beta (Aβ, red) treatment for 6 h. Nuclei were stained with DAPI (blue). Scale bar, 50 μm.
(J) Percentage of $Iba1^+$ $Aβ^+$ microglia after treatment for 6 h with or without 5 mM acetate. Each symbol represents one biological replicate. Data are representative of two independent experiments.
(K) *Cxcl10*, *Ccl5*, and *RelB* mRNA measured by qPCR in microglia from cultured primary microglia challenged or unchallenged with either acetate or monomeric Aβ alone or combined for 6 h. Gene expression was normalized to *β-Actin*. Each symbol represents one biological replicate. Data are representative of two independent experiments.
(L) Percentage of acetate uptake from the media in cultured primary microglia after 6 h incubation time with or without monomeric Aβ. Each symbol represents one biological replicate. Data are representative of two independent experiments.
(M) Fraction of acetate-derived ^{13}C-labeled carbons for various metabolites in primary microglia after 6 h incubation time with or without monomeric Aβ. Data are representative of two independent experiments.
See also Figure S7.

et al., 2016). The effects of gut microbiota on CNS diseases have been documented for several pathologies such as stroke (Benakis et al., 2016), AD (Harach et al., 2017), PD (Sampson et al., 2016), amyotrophic lateral sclerosis (Blacher et al., 2019), and in mouse models for multiple sclerosis (Berer et al., 2011). There are comparable data existing from humans confirming the relevance of these findings from mice (Mossad and Erny, 2020).

Here, we show that the immature microglial phenotype is epigenetically imprinted via altered H3K4me3 and H3K9ac that potentially regulate microglial properties including cellular metabolism. Indeed, we established that the microglial metabolic state *in situ* is essentially modulated by the presence of commensal microorganisms. To date, the metabolic state of microglia *in vivo* has been little studied, and most existing data were obtained from cultured microglia, or from hematopoietic stem cell-derived bone marrow macrophages that represent a different developmental lineage and are therefore not equivalent to microglia (Baik et al., 2019; Borst et al., 2019; Kierdorf et al., 2013; Ulland et al., 2017). By optimizing experimental protocols, we were able to identify several metabolic deficits in microglia isolated from GF mice, such as increased numbers of mitochondria coupled with low $\Delta\psi m$. We believe that differences in microglial mitochondria from GF mice compared to those from SPF mice reflect diminished CII function within the mitochondrial respiratory chain.

SCFAs are known to be able to translocate from the intestine to the systemic circulation and to cross the blood-brain barrier (Frost et al., 2014). They have been reported to have various effects on immune cells including Treg cells (Duscha et al., 2020; Smith et al., 2013) or T effector cells (Qiu et al., 2019) and macrophages (Schulthess et al., 2019; Zhang et al., 2019). In our study, acetate was the most abundant SCFA in the brains of SPF mice and was significantly reduced in brains from GF mice. An accumulation of acetate within the CNS has been described previously in rats (Perry et al., 2016). We showed that gut-derived ^{13}C-acetate reaches the brain and can be metabolized by microglia and other CNS cells and restore observed GF-associated defects in CII function. Despite the clear incorporation of acetate into microglial core metabolism, we cannot exclude additional effects of acetate on protein or histone acetylation, as was shown for T cells (Qiu et al., 2019). Furthermore, acetate, in the form of acetyl-coenzyme A (Ac-CoA), is present in the mitochondria serving as carbon donor in the TCA cycle, production of citrate, and generation of ATP (Cameron et al., 2016). Upon demand, the citrate can exit the mitochondria via the citrate transporter SLC25A1 and be catabolized to Ac-CoA and OAA, mediated by the ATP-citrate lyase (ACL), and finally the Ac-CoA can contribute to nuclear histone and cytoplasmic protein acetylation (Cameron et al., 2016; Covarrubias et al., 2016; Lauterbach et al., 2019). In the current study, it was shown that GF mice have significantly reduced acetate levels in the brain, which was linked to CII-mediated deficiency in microglia, potentially due to elevated OAA concentration. One possible explanation is that microglia in GF mice, in need of acetate (e.g., for protein synthesis and histone acetylation), activate the ACL-mediated conversion of citrate to Ac-CoA at the expense of producing OAA, which partially inhibits CII activity as a competitive inhibitor with a high affinity to the dicarboxylate binding site of CII (Kotlyar and Vinogradov, 1984; Schollmeyer and Klingenberg, 1961). Indeed, from the targeted metabolomic profiling of GF-derived microglia, citrate showed strongly attenuated tendency, although not significant, accompanied with an enrichment of OAA in comparison to SPF controls. Future studies are needed to address this issue and elucidate exactly how acetate affects microglial biology.

In a disease model of AD, we noticed that Aβ pathology can be modulated by host microbiota, which is in accordance with earlier reports (Harach et al., 2017). Remarkably, oral administration of acetate alone was able to modify Aβ burden in the hippocampus of GF 5xFAD mice by modulating microglial phagocytosis rates to those observed in microglia from SPF 5xFAD mice. In other work using GF 5xFAD mice, we ruled out the possibility that processing of the amyloid precursor protein (APP) is affected in the CNS by absent commensals (Mezö et al., 2020). Although we observed that acetate affected metabolic features and enhanced maturation in microglial cells from GF animals, under steady state it suppressed cellular phagocytosis, ultimately leading to an increased Aβ burden in 5xFAD animals. Concomitantly, acetate induced a proinflammatory phenotype of microglia with elevated cytokine expression, which is in turn described to attenuate microglial phagocytosis (Koenigsknecht-Talboo and Landreth, 2005). Notably, in freshly isolated Aβ phagocytosing microglia from 5xFAD mice we observed a metabolic shift with elevated mitochondrial and total ROS as well as oxidative phosphorylation and $\Delta\psi m$. Further, we did not detect dysfunction of CII as observed under healthy conditions in GF housed animals. We speculate that in activated microglial cells the endogenous CII inhibitor OAA might be less abundant since OAA might likely be used for the generation of glucose and other metabolites (Wallace et al., 1998). In contrast, we observed in Aβ phagocytosing microglia from SPF 5xFAD mice increased uptake of glucose compared to GF 5xFAD controls, indicating that glycolysis as the main source for ATP generation is potentially attenuated in phagocytic microglia from GF 5xFAD causing a less pronounced proinflammatory phenotype. In another study, a mixture of SCFAs was reported to be capable of modulating alpha synuclein pathology in a mouse model of PD, and it was suggested that this effect might be mediated by microglia through secretion of proinflammatory cytokines such as IL6 and TNF (Sampson et al., 2016). Therefore, future therapeutic inventions on SCFAs during neurodegeneration should aim to reduce acetate levels in order to ameliorate the course of neurodegeneration. It remains to be shown whether acetate supplementation to older GF 5xFAD affects memory functions as well since we focused in our study on an earlier state of the disease. Moreover, it is currently unclear whether more matured microglial cells might also have a better capacity to deal with any kind of infections that would be vital to keep the relative immune privilege of the brain. Therefore, future experiments are necessary to elucidate the complex roles of acetate for the CNS immune system during health and perturbation.

Limitations of study

Here, we have described an acetate-dependent metabolic state of microglia whereby our data have been generated by using rodent models. Future investigations are necessary to address these findings in human subjects. Indeed, even if the first reports

have already described human microbiome alterations in AD (Cattaneo et al., 2017; Vogt et al., 2017), analysis of this microbiome alteration with a focus on acetate and microglia remains to be performed. In addition, the description of microglial metabolic functions can appear limited here, and more in-depth approaches should be applied to dissect how microglia are integrated into a global metabolic regulation of the organism.

STAR★METHODS

Detailed methods are provided in the online version of this paper and include the following:

- KEY RESOURCES TABLE
- RESOURCE AVAILABILITY
  - Lead contact
  - Materials availability
  - Data and code availability
- EXPERIMENTAL MODEL AND SUBJECT DETAILS
  - Mice
- METHOD DETAILS
  - Histology
  - 3-D reconstruction of microglia
  - Microglia isolation and flow cytometry
  - Metabolic assays
  - Short chain fatty acid (SCFA) quantification
  - *In vivo* and *in vitro* ^{13}C-acetate tracing
  - RNA-sequencing
  - Gene expression analysis
  - ChIP sequencing and qPCR
  - Metabolic profiling
  - Oxaloacetic acid measurement
  - Proteomics
  - Electron microscopy
  - Western blot
- QUANTIFICATION AND STATISTICAL ANALYSIS
  - Statistical analysis

SUPPLEMENTAL INFORMATION

Supplemental information can be found online at https://doi.org/10.1016/j.cmet.2021.10.010.

ACKNOWLEDGMENTS

We thank Eileen Barleon, Tina el Gaz, Katrin Seidel, Sigrun Nestel, and Nena Apollonio for excellent technical assistance. We are grateful to J. Bodinek-Wersing for cell sorting and Catherine Mooser, Bern, for excellent help with the acetate experiments. Metabolic profilings were performed by Daniel Stößel at Metabolic Discoveries Potsdam, Germany, and by Jörg Büscher and the Metabolomics Facility at the MPI-IE, Freiburg, Germany. RNA-seq was performed at KFB, Center of Excellence for Fluorescent Bioanalytics, Regensburg. The Proteomic Platform—Core Facility was supported by the Research Committee (Forschungskommission) of the Faculty of Medicine, University of Freiburg. D.E. is supported by the DFG (SFB/TRR167, ID259373024, A07) and the Berta-Ottenstein-Programme for Advanced Clinician Scientists. T.B. is supported by the DFG (SFB/TRR167, ID259373024, A07). M.P. is supported by the Sobek Foundation, the Ernst-Jung Foundation, the Novo Nordisk Foundation, the DFG (SFB 992, SFB1160, SFB 1479, SFB/TRR167, and Gottfried Wilhelm Leibniz-Prize), and the Ministry of Science, Research and Arts, Baden-Wuerttemberg (Sonderlinie "Neuroinflammation"). M.P. was further supported by the DFG under Germany's Excellence Strategy (CIBSS – EXC-2189 – Project ID 390939984). E.J.P. was supported by the Max-Plank Society and the DFG (SFB 1160 and FOR2599). M.V. was supported by an Alexander von Humboldt Postdoctoral Fellowship and a Young Investigator Fund for Innovative Research Ideas from the Fritz Thyssen Foundation. M.G.d.A. was supported by an Ambizione Grant of the Swiss National Science Foundation (PZ00P3_168012).

AUTHOR CONTRIBUTIONS

D.E., N.D., and C.M. designed and conducted the majority of the experiments. D.E. wrote the manuscript. N.D., C.M., E.J.P., and M.P. edited the manuscript. A.C., M.V., and E.J.P. assisted with Seahorse and tracing experiments and contributed to data analysis and interpretation. O.M., A.M., V.F., J.N., J.S., and T.B. provided help with the tissue processing and experiments. A.M. analyzed TEM data and A.V. helped with TEM analysis. D.E., M.F., and O. Staszewski analyzed the RNA-seq and ChIP-seq data. S.T. and O. Schilling performed proteomics. M.G.d.A. and A.J.M. bred GF animals and performed SCFA treatment. D.E. and M.P. conceptualized and supervised the project.

DECLARATION OF INTERESTS

The authors declare no competing interests.

Received: April 20, 2021
Revised: August 12, 2021
Accepted: October 13, 2021
Published: November 2, 2021

REFERENCES

Amit, I., Winter, D.R., and Jung, S. (2016). The role of the local environment and epigenetics in shaping macrophage identity and their effect on tissue homeostasis. Nat. Immunol. *17*, 18–25.

Andrews, S. (2019). FastQC: a quality control tool for high throughput sequence data.

Babcock, A.A., Ilkjær, L., Clausen, B.H., Villadsen, B., Dissing-Olesen, L., Bendixen, A.T., Lyck, L., Lambertsen, K.L., and Finsen, B. (2015). Cytokine-producing microglia have an altered beta-amyloid load in aged APP/PS1 Tg mice. Brain Behav. Immun. *48*, 86–101.

Baik, S.H., Kang, S., Lee, W., Choi, H., Chung, S., Kim, J.I., and Mook-Jung, I. (2019). A breakdown in metabolic reprogramming causes microglia dysfunction in Alzheimer's disease. Cell Metab. *30*, 493–507.e6.

Benakis, C., Brea, D., Caballero, S., Faraco, G., Moore, J., Murphy, M., Sita, G., Racchumi, G., Ling, L., Pamer, E.G., et al. (2016). Commensal microbiota affects ischemic stroke outcome by regulating intestinal γδ T cells. Nat. Med. *22*, 516–523.

Benjamini, Y., and Hochberg, Y. (1995). Controlling the false discovery rate: a practical and powerful approach to multiple testing. J. R. Stat. Soc. B. *57*, 289–300.

Berer, K., Mues, M., Koutrolos, M., Rasbi, Z.A., Boziki, M., Johner, C., Wekerle, H., and Krishnamoorthy, G. (2011). Commensal microbiota and myelin autoantigen cooperate to trigger autoimmune demyelination. Nature *479*, 538–541.

Blacher, E., Bashiardes, S., Shapiro, H., Rothschild, D., Mor, U., Dori-Bachash, M., Kleimeyer, C., Moresi, C., Harnik, Y., Zur, M., et al. (2019). Potential roles of gut microbiome and metabolites in modulating ALS in mice. Nature *572*, 474–480.

Borst, K., Schwabenland, M., and Prinz, M. (2019). Microglia metabolism in health and disease. Neurochem. Int. *130*, 104331.

Buescher, J.M., Antoniewicz, M.R., Boros, L.G., Burgess, S.C., Brunengraber, H., Clish, C.B., DeBerardinis, R.J., Feron, O., Frezza, C., Ghesquiere, B., et al. (2015). A roadmap for interpreting (13)C metabolite labeling patterns from cells. Curr. Opin. Biotechnol. *34*, 189–201.

Cameron, A.M., Lawless, S.J., and Pearce, E.J. (2016). Metabolism and acetylation in innate immune cell function and fate. Semin. Immunol. *28*, 408–416.

Caputa, G., Castoldi, A., and Pearce, E.J. (2019). Metabolic adaptations of tissue-resident immune cells. Nat. Immunol. *20*, 793–801.

Cattaneo, A., Cattane, N., Galluzzi, S., Provasi, S., Lopizzo, N., Festari, C., Ferrari, C., Guerra, U.P., Paghera, B., Muscio, C., et al.; INDIA-FBP Group (2017). Association of brain amyloidosis with pro-inflammatory gut bacterial taxa and peripheral inflammation markers in cognitively impaired elderly. Neurobiol. Aging *49*, 60–68.

Colonna, M., and Butovsky, O. (2017). Microglia function in the central nervous system during health and neurodegeneration. Annu. Rev. Immunol. *35*, 441–468.

Covarrubias, A.J., Aksoylar, H.I., Yu, J., Snyder, N.W., Worth, A.J., Iyer, S.S., Wang, J., Ben-Sahra, I., Byles, V., Polynne-Stapornkul, T., et al. (2016). Akt-mTORC1 signaling regulates Acly to integrate metabolic input to control of macrophage activation. eLife *5*, e11612.

Cryan, J.F., O'Riordan, K.J., Cowan, C.S.M., Sandhu, K.V., Bastiaanssen, T.F.S., Boehme, M., Codagnone, M.G., Cussotto, S., Fulling, C., Golubeva, A.V., et al. (2019). The microbiota-gut-brain axis. Physiol. Rev. *99*, 1877–2013.

Datta, M., Staszewski, O., Raschi, E., Frosch, M., Hagemeyer, N., Tay, T.L., Blank, T., Kreutzfeldt, M., Merkler, D., Ziegler-Waldkirch, S., et al. (2018). Histone deacetylases 1 and 2 regulate microglia function during development, homeostasis, and neurodegeneration in a context-dependent manner. Immunity *48*, 514–529.e6.

Dobin, A., Davis, C.A., Schlesinger, F., Drenkow, J., Zaleski, C., Jha, S., Batut, P., Chaisson, M., and Gingeras, T.R. (2013). STAR: ultrafast universal RNA-seq aligner. Bioinformatics *29*, 15–21.

Duscha, A., Gisevius, B., Hirschberg, S., Yissachar, N., Stangl, G.I., Eilers, E., Bader, V., Haase, S., Kaisler, J., David, C., et al. (2020). Propionic acid shapes the multiple sclerosis disease course by an immunomodulatory mechanism. Cell *180*, 1067–1080.e16.

Erny, D., and Prinz, M. (2017). Microbiology: gut microbes augment neurodegeneration. Nature *544*, 304–305.

Erny, D., and Prinz, M. (2020). How microbiota shape microglial phenotypes and epigenetics. Glia *68*, 1655–1672.

Erny, D., Hrabě de Angelis, A.L., Jaitin, D., Wieghofer, P., Staszewski, O., David, E., Keren-Shaul, H., Mahlakoiv, T., Jakobshagen, K., Buch, T., et al. (2015). Host microbiota constantly control maturation and function of microglia in the CNS. Nat. Neurosci. *18*, 965–977.

Frankish, A., Diekhans, M., Ferreira, A.M., Johnson, R., Jungreis, I., Loveland, J., Mudge, J.M., Sisu, C., Wright, J., Armstrong, J., et al. (2019). GENCODE reference annotation for the human and mouse genomes. Nucleic Acids Res. *47* (D1), D766–D773.

Frost, G., Sleeth, M.L., Sahuri-Arisoylu, M., Lizarbe, B., Cerdan, S., Brody, L., Anastasovska, J., Ghourab, S., Hankir, M., Zhang, S., et al. (2014). The short-chain fatty acid acetate reduces appetite via a central homeostatic mechanism. Nat. Commun. *5*, 3611.

Garzetti, D., Brugiroux, S., Bunk, B., Pukall, R., McCoy, K.D., Macpherson, A.J., and Stecher, B. (2017). High-quality whole-genome sequences of the oligo-mouse-microbiota bacterial community. Genome Announc. *5*, e00758-17.

Gosselin, D., Link, V.M., Romanoski, C.E., Fonseca, G.J., Eichenfield, D.Z., Spann, N.J., Stender, J.D., Chun, H.B., Garner, H., Geissmann, F., and Glass, C.K. (2014). Environment drives selection and function of enhancers controlling tissue-specific macrophage identities. Cell *159*, 1327–1340.

Hagemeyer, N., Hanft, K.M., Akriditou, M.A., Unger, N., Park, E.S., Stanley, E.R., Staszewski, O., Dimou, L., and Prinz, M. (2017). Microglia contribute to normal myelinogenesis and to oligodendrocyte progenitor maintenance during adulthood. Acta Neuropathol. *134*, 441–458.

Haghikia, A., Jörg, S., Duscha, A., Berg, J., Manzel, A., Waschbisch, A., Hammer, A., Lee, D.H., May, C., Wilck, N., et al. (2015). Dietary fatty acids directly impact central nervous system autoimmunity via the small intestine. Immunity *43*, 817–829.

Harach, T., Marungruang, N., Duthilleul, N., Cheatham, V., Mc Coy, K.D., Frisoni, G., Neher, J.J., Fåk, F., Jucker, M., Lasser, T., and Bolmont, T. (2017). Reduction of Abeta amyloid pathology in APPPS1 transgenic mice in the absence of gut microbiota. Sci. Rep. *7*, 41802.

Heberle, H., Meirelles, G.V., da Silva, F.R., Telles, G.P., and Minghim, R. (2015). InteractiVenn: a web-based tool for the analysis of sets through Venn diagrams. BMC Bioinformatics *16*, 169.

Jin, Y.Y., Shi, Z.Q., Chang, W.Q., Guo, L.X., Zhou, J.L., Liu, J.Q., Liu, L.F., and Xin, G.Z. (2018). A chemical derivatization based UHPLC-LTQ-Orbitrap mass spectrometry method for accurate quantification of short-chain fatty acids in bronchoalveolar lavage fluid of asthma mice. J. Pharm. Biomed. Anal. *161*, 336–343.

Keren-Shaul, H., Spinrad, A., Weiner, A., Matcovitch-Natan, O., Dvir-Szternfeld, R., Ulland, T.K., David, E., Baruch, K., Lara-Astaiso, D., Toth, B., et al. (2017). A unique microglia type associated with restricting development of Alzheimer's disease. Cell *169*, 1276–1290.e17.

Kierdorf, K., Erny, D., Goldmann, T., Sander, V., Schulz, C., Perdiguero, E.G., Wieghofer, P., Heinrich, A., Riemke, P., Hölscher, C., et al. (2013). Microglia emerge from erythromyeloid precursors via Pu.1- and Irf8-dependent pathways. Nat. Neurosci. *16*, 273–280.

Kindt, A., Liebisch, G., Clavel, T., Haller, D., Hörmannsperger, G., Yoon, H., Kolmeder, D., Sigruener, A., Krautbauer, S., Seeliger, C., et al. (2018). The gut microbiota promotes hepatic fatty acid desaturation and elongation in mice. Nat. Commun. *9*, 3760.

Koenigsknecht-Talboo, J., and Landreth, G.E. (2005). Microglial phagocytosis induced by fibrillar beta-amyloid and IgGs are differentially regulated by proinflammatory cytokines. J. Neurosci. *25*, 8240–8249.

Kotlyar, A.B., and Vinogradov, A.D. (1984). Interaction of the membrane-bound succinate dehydrogenase with substrate and competitive inhibitors. Biochim. Biophys. Acta *784*, 24–34.

Lauterbach, M.A., Hanke, J.E., Serefidou, M., Mangan, M.S.J., Kolbe, C.C., Hess, T., Rothe, M., Kaiser, R., Hoss, F., Gehlen, J., et al. (2019). Toll-like receptor signaling rewires macrophage metabolism and promotes histone acetylation via ATP-citrate lyase. Immunity *51*, 997–1011.e7.

Lavin, Y., Winter, D., Blecher-Gonen, R., David, E., Keren-Shaul, H., Merad, M., Jung, S., and Amit, I. (2014). Tissue-resident macrophage enhancer landscapes are shaped by the local microenvironment. Cell *159*, 1312–1326.

Law, C.W., Chen, Y., Shi, W., and Smyth, G.K. (2014). voom: precision weights unlock linear model analysis tools for RNA-seq read counts. Genome Biol. *15*, R29.

Li, Q., and Barres, B.A. (2018). Microglia and macrophages in brain homeostasis and disease. Nat. Rev. Immunol. *18*, 225–242.

Liao, Y., Smyth, G.K., and Shi, W. (2014). featureCounts: an efficient general purpose program for assigning sequence reads to genomic features. Bioinformatics *30*, 923–930.

Liu, R., Holik, A.Z., Su, S., Jansz, N., Chen, K., Leong, H.S., Blewitt, M.E., Asselin-Labat, M.L., Smyth, G.K., and Ritchie, M.E. (2015). Why weight? Modelling sample and observational level variability improves power in RNA-seq analyses. Nucleic Acids Res. *43*, e97.

Meyer-Luehmann, M., and Prinz, M. (2015). Myeloid cells in Alzheimer's disease: culprits, victims or innocent bystanders? Trends Neurosci. *38*, 659–668.

Mezö, C., Dokalis, N., Mossad, O., Staszewski, O., Neuber, J., Yilmaz, B., Schnepf, D., de Agüero, M.G., Ganal-Vonarburg, S.C., Macpherson, A.J., et al. (2020). Different effects of constitutive and induced microbiota modulation on microglia in a mouse model of Alzheimer's disease. Acta Neuropathol. Commun. *8*, 119.

Mildner, A., Schlevogt, B., Kierdorf, K., Böttcher, C., Erny, D., Kummer, M.P., Quinn, M., Brück, W., Bechmann, I., Heneka, M.T., et al. (2011). Distinct and non-redundant roles of microglia and myeloid subsets in mouse models of Alzheimer's disease. J. Neurosci. *31*, 11159–11171.

Mossad, O., and Erny, D. (2020). The microbiota-microglia axis in central nervous system disorders. Brain Pathol. *30*, 1159–1177.

O'Sullivan, D., Sanin, D.E., Pearce, E.J., and Pearce, E.L. (2019). Metabolic interventions in the immune response to cancer. Nat. Rev. Immunol. *19*, 324–335.

Perry, R.J., Peng, L., Barry, N.A., Cline, G.W., Zhang, D., Cardone, R.L., Petersen, K.F., Kibbey, R.G., Goodman, A.L., and Shulman, G.I. (2016).

Acetate mediates a microbiome-brain-β-cell axis to promote metabolic syndrome. Nature *534*, 213–217.

Prinz, M., Priller, J., Sisodia, S.S., and Ransohoff, R.M. (2011). Heterogeneity of CNS myeloid cells and their roles in neurodegeneration. Nat. Neurosci. *14*, 1227–1235.

Prinz, M., Jung, S., and Priller, J. (2019). Microglia biology: one century of evolving concepts. Cell *179*, 292–311.

Qiu, J., Villa, M., Sanin, D.E., Buck, M.D., O'Sullivan, D., Ching, R., Matsushita, M., Grzes, K.M., Winkler, F., Chang, C.H., et al. (2019). Acetate promotes T cell effector function during glucose restriction. Cell Rep. *27*, 2063–2074.e5.

Raasch, J., Zeller, N., van Loo, G., Merkler, D., Mildner, A., Erny, D., Knobeloch, K.P., Bethea, J.R., Waisman, A., Knust, M., et al. (2011). IkappaB kinase 2 determines oligodendrocyte loss by non-cell-autonomous activation of NF-kappaB in the central nervous system. Brain *134*, 1184–1198.

Raivo, K. (2019). pheatmap: Pretty Heatmaps. R package version 1.0.12.

Ramírez, F., Dündar, F., Diehl, S., Grüning, B.A., and Manke, T. (2014). deepTools: a flexible platform for exploring deep-sequencing data. Nucleic Acids Res. *42*, W187–W191.

Robinson, J.T., Thorvaldsdóttir, H., Winckler, W., Guttman, M., Lander, E.S., Getz, G., and Mesirov, J.P. (2011). Integrative genomics viewer. Nat. Biotechnol. *29*, 24–26.

Salabei, J.K., Gibb, A.A., and Hill, B.G. (2014). Comprehensive measurement of respiratory activity in permeabilized cells using extracellular flux analysis. Nat. Protoc. *9*, 421–438.

Sampson, T.R., Debelius, J.W., Thron, T., Janssen, S., Shastri, G.G., Ilhan, Z.E., Challis, C., Schretter, C.E., Rocha, S., Gradinaru, V., et al. (2016). Gut microbiota regulate motor deficits and neuroinflammation in a model of Parkinson's disease. Cell *167*, 1469–1480.e12.

Sanin, D.E., Matsushita, M., Klein Geltink, R.I., Grzes, K.M., van Teijlingen Bakker, N., Corrado, M., Kabat, A.M., Buck, M.D., Qiu, J., Lawless, S.J., et al. (2018). Mitochondrial membrane potential regulates nuclear gene expression in macrophages exposed to prostaglandin E2. Immunity *49*, 1021–1033.e6.

Sarlus, H., and Heneka, M.T. (2017). Microglia in Alzheimer's disease. J. Clin. Invest. *127*, 3240–3249.

Schollmeyer, P., and Klingenberg, M. (1961). Oxaloacetate and adenosinetriphosphate levels during inhibition and activation of succinate oxidation. Biochem. Biophys. Res. Commun. *4*, 43–47.

Schulthess, J., Pandey, S., Capitani, M., Rue-Albrecht, K.C., Arnold, I., Franchini, F., Chomka, A., Ilott, N.E., Johnston, D.G.W., Pires, E., et al. (2019). The short chain fatty acid butyrate imprints an antimicrobial program in macrophages. Immunity *50*, 432–445.e7.

Shen, L., Shao, N.-Y., Liu, X., Maze, I., Feng, J., and Nestler, E.J. (2013). diffReps: detecting differential chromatin modification sites from ChIP-seq data with biological replicates. PLoS ONE *8*, e65598.

Smith, P.M., Howitt, M.R., Panikov, N., Michaud, M., Gallini, C.A., Bohlooly-Y, M., Glickman, J.N., and Garrett, W.S. (2013). The microbial metabolites, short-chain fatty acids, regulate colonic Treg cell homeostasis. Science *341*, 569–573.

Sofer, A., Lei, K., Johannessen, C.M., and Ellisen, L.W. (2005). Regulation of mTOR and cell growth in response to energy stress by REDD1. Mol. Cell. Biol. *25*, 5834–5845.

Stoessel, D., Stellmann, J.-P., Willing, A., Behrens, B., Rosenkranz, S.C., Hodecker, S.C., Stürner, K.H., Reinhardt, S., Fleischer, S., Deuschle, C., et al. (2018). Metabolomic profiles for primary progressive multiple sclerosis stratification and disease course monitoring. Front. Hum. Neurosci. *12*, 226.

Thion, M.S., Low, D., Silvin, A., Chen, J., Grisel, P., Schulte-Schrepping, J., Blecher, R., Ulas, T., Squarzoni, P., Hoeffel, G., et al. (2018). Microbiome influences prenatal and adult microglia in a sex-specific manner. Cell *172*, 500–516.e16.

Uchimura, Y., Wyss, M., Brugiroux, S., Limenitakis, J.P., Stecher, B., McCoy, K.D., and Macpherson, A.J. (2016). Complete genome sequences of 12 species of stable defined moderately diverse mouse microbiota 2. Genome Announc. *4*, e00951-16.

Ulland, T.K., Song, W.M., Huang, S.C., Ulrich, J.D., Sergushichev, A., Beatty, W.L., Loboda, A.A., Zhou, Y., Cairns, N.J., Kambal, A., et al. (2017). TREM2 maintains microglial metabolic fitness in Alzheimer's disease. Cell *170*, 649–663.e13.

Vogt, N.M., Kerby, R.L., Dill-McFarland, K.A., Harding, S.J., Merluzzi, A.P., Johnson, S.C., Carlsson, C.M., Asthana, S., Zetterberg, H., Blennow, K., et al. (2017). Gut microbiome alterations in Alzheimer's disease. Sci. Rep. *7*, 13537.

Wallace, J.C., Jitrapakdee, S., and Chapman-Smith, A. (1998). Pyruvate carboxylase. Int. J. Biochem. Cell Biol. *30*, 1–5.

Wendeln, A.C., Degenhardt, K., Kaurani, L., Gertig, M., Ulas, T., Jain, G., Wagner, J., Häsler, L.M., Wild, K., Skodras, A., et al. (2018). Innate immune memory in the brain shapes neurological disease hallmarks. Nature *556*, 332–338.

Zhang, Z., Tang, H., Chen, P., Xie, H., and Tao, Y. (2019). Demystifying the manipulation of host immunity, metabolism, and extraintestinal tumors by the gut microbiome. Signal Transduct. Target. Ther. *4*, 41.

STAR★METHODS

KEY RESOURCES TABLE

REAGENT or RESOURCE	SOURCE	IDENTIFIER
Antibodies		
Rabbit anti-Iba-1	Wako	Cat# 01919741; RRID: AB_839504
Rabbit anti-Tomm20	Abcam	Cat# ab186734; RRID: AB_2716623
Guinea pig anti-Iba1	Synaptic Systems	Cat# 234004; RRID: AB_2493179
Alexa Flour 488-conjugated Donkey anti-Rat	Thermo Fisher Scientific	Cat# A21208; RRID: AB_2535794
Alexa Fluor 488-Donkey anti-Goat	Thermo Fisher Scientific	Cat# A11055; RRID: AB_2534102
Alexa Flour 568-conjugated Donkey anti-Mouse	Thermo Fisher Scientific	Cat# A10037; RRID: AB_2534013
Alexa Fluor 568 goat anti Guinea pig	Thermo Fisher Scientific	Cat# A11075; RRID: AB_2534119
Alexa Fluor 647-conjugated Donkey anti-Rabbit	Thermo Fisher Scientific	Cat# A31573; RRID: AB_2536183
Rat anti-mouse CD11b APC conjugated	Thermo Fisher Scientific	Cat# 17-0112-83; RRID: AB_469344
Rat anti-mouse CD19 PE-Cy7 conjugated	Biolegend	Cat# 115520; RRID: AB_313655
Rat anti-mouse CD3 PE-Cy7 conjugated	Biolegend	Cat# 100219; RRID: AB_1732068
Rat anti-mouse CD45 PE conjugated	Thermo Fisher Scientific	Cat# 12-0451-83; RRID: AB_465669
Rat anti-mouse CD45 PE-Cy7 conjugated	Thermo Fisher Scientific	Cat# 25-0451-82; RRID: AB_2734986
Rat anti-mouse CD45R PE-Cy7 conjugated	Biolegend	Cat# 103222; RRID: AB_313005
Rat anti-mouse Ly6C PE-Cy7 conjugated	BD Bioscience	Cat# 560593; RRID: AB_1727557
Rat anti-mouse Ly6G PE-Cy7 conjugated	BD Bioscience	Cat# 560601; RRID: AB_1727562
FC receptor blocking antibody CD16/CD32	BD Bioscience	Cat# 564219; RRID: AB_2728082
HRP Anti-beta Actin	Abcam	Cat# 20272
Mitochondrial Marker Antibody Sampler Kit	Cell Signaling	Cat# 8674T
Chemicals, peptides, and recombinant proteins		
2-NBDG (2-(N-(7-Nitrobenz-2-oxa-1,3-diazol-4- yl)Amino)-2-Desoxyglucose)	ThermoFisher Scientific	Cat# N13195
CellROX Deep Red Reagent	ThermoFisher Scientific	Cat# C10422
DAPI (4',6-Diamidino-2-Phenylindole)	Carl Roth	Cat# 6335.2
eBioscience Fixable Viabitity Dye eFluor 780	ThermoFisher Scientific	Cat# 65-0865-14
Methoxy-XO4	Tocris	Cat# 4920
MitoSOX Red Reagent	ThermoFisher Scientific	Cat# M36008
MitoTracker Green FM	ThermoFisher Scientific	Cat# M7514
Thiazine Red	Sigma-Aldrich	Cat# S570435-1G
TMRM (tetramethyl-rhodamine methyl ester)	ThermoFisher Scientific	Cat# T668
BODIPY 493/503 (4,4-Difluoro-1,3,5,7,8-Pentamethyl4-Bora-3a,4a-Diaza-s-Indacen)	ThermoFisher Scientific	Cat# D3922
LysoTracker Deep Red	ThermoFisher Scientific	Cat# L12492
Seahorse XF Plasma Membrane Permeabilizer	Agilent	Cat# 102504-100
Sodium Acetate (1-13C, 99%)	Cambridge Isotome Laboratories	Cat# 23424-28-4
Beta-Amyloid	Anaspec	Cat# AS-20276
RapiGest SF Surfactant	Waters	Cat# 186002122
HQ SILVER	Nanoprobes	Cat# 2012
SuperSignal Western Blot	ThermoFisher Scientific	Cat# A43841
Sodium acetate (1,2-13C2, 99%)	Cambridge Isotope Laboratories	Cat# CLM-440-1
Critical commercial assays		
Acetate V2 Bio	Roche	Cat# 07395442001
PicoPure RNA Isolation Kit	ThermoFisher Scientific	Cat# KIT0204
SMARTer v4 Ultra Low Input RNA Kit for Sequencing	Clontech Laboratories	Cat# 634893

(*Continued on next page*)

Continued

REAGENT or RESOURCE	SOURCE	IDENTIFIER
Illumina TruSeq SR Cluster Kit v3	Illumina	Cat# GD-401-3001
KAPA Library Quantification Kit	Roche	Cat# 07960140001
TruSeq SBS Kit v3-HS	Illumina	Cat# FC-401-3001
Nextera XT DNA Library Preparation Kit	Illumina	Cat# FC-131-1024
High-Capacity RNA-to-cDNA Kit	ThermoFisher Scientific	Cat# 4387406
True MicroChIP-seq Kit	Diagenode	Cat# C01010132
Deproteinizing Sample Preparation Kit – TCA	Abcam	Cat# ab204708
Oxaloacetate Assay Kit	Abcam	Cat# ab83428
Deposited data		
RNA- and ChIP-sequencing data	This paper	GEO: GSE184881
Proteome data	This paper	MassIVE (PXD028459)
Experimental models: Organisms/strains		
Mouse: C57BL/6J GF	University Hospital Bern, Switzerland	N/A
Mouse: C57BL/6J SPF	Janvier labs, France	N/A
5xFAD	inhouse breeding (CEMT, Freiburg, Germany)	N/A
Software and algorithms		
FlowJo software	TreeStar	https://www.flowjo.com/
IMARIS software	Bitplane	https://imaris.oxinst.com
BZII-Analyzer	Keyence	N/A
GraphPad Prism 5	GraphPad	N/A
Image Lab Software Version 5.0	Bio-Rad	N/A
Ingenuity Pathway Analysis	QIAGEN	N/A

RESOURCE AVAILABILITY

Lead contact

Further information and requests for resources and reagents should be directed to and will be fulfilled by the lead contact Marco Prinz, marco.prinz@uniklinik-freiburg.de.

Materials availability

This study did not generate new unique reagents.

Data and code availability

RNA-, ChIP-seq and proteomics data have been deposited at GEO and are publicly available as of the date of publication. Accession numbers are listed in the key resources table. Any additional information required to reanalyze the data reported in this paper is available from the lead contact upon request.

EXPERIMENTAL MODEL AND SUBJECT DETAILS

Mice

Conventional SPF housed wildtype (WT) mice on C57BL/6 background were purchased from Janvier labs (Saint Berthevin, France). Germ-free WT mice were obtained from the Clean Mouse Facility (Bern, Switzerland). WT mice (mixed sex) were used at 6–12 weeks of age. 5xFAD mice were housed under SPF conditions at CEMT (Freiburg, Germany) and under GF conditions at Clean Mouse Facility (Bern, Switzerland). Male 5xFAD mice on C57BL/6 background and negative litters were used at an age of 16 weeks. For treatment with short-chain fatty acids (SCFA), either sodium acetate (150 mM), sodium propionate (150 mM), sodium butyrate (100 mM) or a SCFA mix (67.5 mM acetate, 40 mM Butyrate, 25.9 mM Propionate) (Sigma-Aldrich, Taufkirchen, Germany) were added to drinking water as described previously (Erny et al., 2015; Smith et al., 2013). Under steady-state conditions, mice were treated with SCFA for four weeks prior to analysis. 5xFAD mice and WT controls were treated for 8 weeks with acetate prior to analysis. Sodium matched water was applied to control mice. Water solutions were prepared and changed weekly. In order to deplete gut microbiota, C57BL/6 mice were treated orally via drinking water with a mixture of antibiotics (ABX), containing 1 mg/mL vancomycin (Hexal), 1 mg/mL

cefoxitin (Santa Cruz Biotechnology), 1 mg/mL gentamicin (Sigma-Aldrich) and 1 mg/mL metronidazol (Sigma-Aldrich) for 4 weeks as described previously (Erny et al., 2015). To study the impact of postnatal recolonization, GF mice were cohoused with adult female SPF-donors upon birth in individually ventilated cages (IVC) cages. Mice with a stable defined moderately diverse mouse microbiota (sDMDMm2) (Uchimura et al., 2016), also known as Oligo-MM^{12} (Garzetti et al., 2017) were obtained from Andrew Macpherson and Mercedes Gomez de Aguero (DBMR, Bern, Switzerland). All animal experiments were approved by the Ministry for Nature, Environment and Consumers' Protection of the state of Baden-Württemberg and were performed in accordance to the respective national, federal and institutional regulations (G19–02, G19-148 and X16-04A).

METHOD DETAILS

Histology

Histology was performed as described recently (Erny et al., 2015). Brains were removed and fixed in 4% phosphate-buffered formalin. Brain tissue was dissected and parasagittal sections were embedded in paraffin before staining with Iba1 (Wako, Osaka, Japan) for microglia. At least 3-4 parasagittal brain sections per mouse were evaluated using Bresser MikroCamLabII (Bresser, Rhede, Germany).

For immunofluorescence labeling 25 μm coronal cryo sections from adult brain tissue were prepared and incubated free-floating first with anti-Iba1 antibody (Wako, Osaka, Japan) for 24 h (dilution 1:500 at 4°C).Subsequently Alexa Fluor-488-conjugated secondary antibody (Life technologies, Darmstadt, Germany) was added at a dilution of 1:500 for 24 h at 4°C. Nuclei were counterstained with 4,6-diamidino-2-phenylindole (DAPI). 2 μM Thiazine red was applied for 5min at room temperature. Every tenth sections from ventral to dorsal hippocampus per individual mouse were examined. Images were taken with BZ-9000 Biorevo microscope (Keyence, Neu-Isenburg, Germany) and the number of Iba1-positive cells and TR-positive plaques were determined using BZ-II Analyzer (Keyence, Neu-Isenburg, Germany).

3-D reconstruction of microglia

30 μm parasagittal cryo sections from adult brain tissue were stained with anti-Iba1 (Wako, Osaka, Japan) for 48 h (dilution 1:500 at 4°C), followed by Alexa Fluor 568–conjugated secondary antibody (Life technologies, Darmstadt, Germany) staining, which was added at a dilution of 1:500 overnight at 4°C. Nuclei were counterstained with DAPI. Imaging was performed on an Olympus Fluoview 1000 confocal laser scanning microscope (Olympus, Hamburg, Germany) using a 20 × 0.95 NA objective. Z stacks were done with 1.14-μm steps in z direction, 1,024 × 1,024 pixel resolution were recorded and analyzed using IMARIS software (Bitplane, Zurich, Switzerland). At least three cortical cells were reconstructed per mouse.

For the 3-D reconstruction of microglial mitochondria 25 μm coronal cryo sections from adult brain tissue were stained with anti-Iba1 (Synaptic systems, Göttingen, Germany) at a dilution of 1:500 and anti-Tomm20 antibody (Abcam, Cambridge, UK) at a dilution of 1:100 for 48 h at 4°C followed by Alexa Fluor 568- and 647-conjugated secondary antibody (Life technologies, Darmstadt, Germany) staining, which was added at a dilution of 1:500 overnight at 4°C. Nuclei were counterstained with DAPI. Imaging was performed on an Leica SP8 confocal laser scanning microscope (Leica, Wetzlar, Germany) using a 63 × 0.95 NA objective. Z stacks were done with system optimized steps in z direction, 1,024 × 1,024 pixel resolution were recorded and analyzed using IMARIS software (Bitplane, Zurich, Switzerland). At least three cortical cells were reconstructed per mouse.

Microglia isolation and flow cytometry

Adult microglia were harvested using density gradient separation and were prepared as described before with slight modifications (Erny et al., 2015). In short, cells were stained with primary antibodies directed against CD11b, CD45, and F4/80 (eBioscience, San Diego, USA) at 4°C for 15 min. Viable single microglia cells were washed and analyzed using a BD FACS Canto or LSRFortessa (Becton Dickinson, Heidelberg, Germany) were sorted with a MoFlo Astrios (Beckman Coulter, Krefeld, Germany) or BD FACSAria III (Becton Dickinson, Heidelberg, Germany) and further processed. Data were acquired with FACSdiva software (Becton Dickinson, Heidelberg, Germany) and were analyzed by using FlowJo software (Tree Star, Ashland, USA).

Metabolic assays

Mitochondrial mass, mitochondrial membrane potential ($\Delta\psi m$) and cellular ROS were measured by incubating at 37°C for 30 min in FACS buffer with 20 nM MitoTracker Green FM (ThermoFisher), 50 nM Tetramethylrhodamine, Methyl Ester, Perchlorate (TMRM) (ThermoFisher) and 5 μM CellROX Deep Red (ThermoFisher), respectively. Mitochondria ROS was determined by incubating at 37°C with 5 μM MitoSox (ThermoFisher) for 10 min in HBSS. Lipid accumulation and lysosomal content were evaluated by incubating in 37°C with 1 μM Bodipy 493/503 (ThermoFisher) for 5 min in PBS and 50 nM LysoTracker DeepRed for 30min in FACS buffer. Glucose uptake was measured by incubating at 37°C with 100 μM 2NBDG (ThermoFisher) for 30 min.

Real time measurement of electron transport chain (ETC) complex activity of microglia was performed as described previously (Sanin et al., 2018) with minor modifications. In brief, cells were stained with the Fixable Viability Dye eFluor 780 (eBioscience), CD11b and CD45 followed by an incubation at 37°C with 20 nM MitoTracker Green FM and 50 nM TMRM for 30 min. Prior to recording the cells were resuspended in MAS-BSA buffer (220 mM mannitol, 70 mM sucrose, 10mM KH_2PO_4, 5mM $MgCl_2$, 2mM HEPES, 1mM EDTA and 0.2% (w/v) bovine serum albumin) as described before (Salabei et al., 2014) with the addition of 50 nM TMRM, 1 nM Agilent Seahorse XF Plasma Membrane Permeabilizer (Agilent) and 1 mM adenosine diphosphate (Sigma-Aldrich). The samples

were measured using a BD FACS Canto and a custom-made sample holder to maintain the temperature at 37°C. The TMRM intensity was recorded while the cells were sequentially treated with 1 μM rotenone (Sigma), 10 mM sodium succinate (Sigma), 20 μM antimycin A (Sigma) or with 5 mM pyruvate/ 2.5mM malate (Sigma), 1 μM carbonyl cyanide 4-(trifluoromethoxy)phenylhydrazone (FCCP) or with 1 μM rotenone, oxaloacetatic acid (OAA) (concentration as indicated, pH corrected) (Sigma), 10 mM sodium succinate. The data were analyzed using FlowJo software (FlowJo).

Real-time ECAR and OCR measurements were made with an XF-96 Extracellular Flux Analyzer (Seahorse Bioscience). 3×10^5 sorted microglia, or 1.5×10^5 sorted peritoneal macrophages, were plated into each well of Seahorse X96 cell culture microplates (coated with poly-L-lysine) and preincubated at 37 °C for a minimum of 45 min in the absence of CO_2 in unbuffered RPMI with 1 mM pyruvate, 2 mM L-glutamine and 25 mM glucose for the mitochondrial stress test, with pH adjusted to 7.4. OCR and ECAR were measured under basal conditions and after the addition of the following compounds: 1 μM oligomycin (Sigma), 1.5 μM FCCP, 100 nM rotenone /1 μM antimycin as indicated. For the glycolysis stress test, the ECAR and OCR were measured under basal conditions and after the sequential treatment with: 10 mM glucose, 1 μM oligomycin, 50 mM 2-deoxyglucose (2-DG) as indicated. Results were collected with Wave software version 2.4 (Agilent).

Short chain fatty acid (SCFA) quantification

To measure the amount of SCFA in the tissue, 200 mg of snap frozen tissue or 50 μL of serum was homogenized in 500 μL of cold (4°C) MS grade H_2O and centrifuged at 10.000 G for 5 min. The supernatant was collected, aliquoted in 100 μL aliquots and stored in −80 freezer. 100 μL of supernatant was used for SCFA measurements by LC-MS using the Agilent 6495 Triple Quad QQQ-MS with 3-nitrophenylhydrazine derivatization as described previously (Jin et al., 2018), with minor modifications. Peak areas were identified based on standards for each SCFA and calculated using MassHunter (Agilent).

In order to quantify the concentration acetate (C2, 59), propionate (C3, 73), and butyrate (and isobutyrate, C4, 87), in SPF, GF and sDMDMm2 mice 10 μL of each mouse blood serum sample was transferred to four eppis. Afterward 90 μL of ACN was added with serial dilution (4 levels) of standards.

	L1	L2	L3	L4
C2/(mg/mL)	0	0.002	0.004	0.006
C3/(mg/mL)	0	0.0002	0.0004	0.0006
C4/(mg/mL)	0	0.0005	0.001	0.0015
C5/%	0	0.000025%	0.00005%	0.000075%

The samples were centrifuged at 20000 g for 10 min at 4°C. 50 μL of each sample was transferred for HPLC-QTOF analysis. 2 μL of each sample was injected. Each sample was analyzed two times and average value was used to build the regression line and calculate the concentration.

Standard addition method: (one point calculation)

$$\frac{C(unknown)}{C(unknown)+C(standard)} = \frac{Signal(unknown)}{Signal(unknown+standard)}$$

Regression: (using more points)

$$y = ax+b$$

$$C(unknown) = b/a$$

In vivo and *in vitro* ^{13}C-acetate tracing

0.1 g ^{13}C-acetate (Cambridge Isotope Laboratories) diluted in 200 μl 0,9% NaCl was applied via oral gavage, as previously described (Kindt et al., 2018). After an incubation time of 6 or 12 h. ^{13}C incorporation in the metabolites of the different tissues and serum were measured by GS-MS (Qiu et al., 2019). The tissue samples were weighted before further processing. The samples were extracted with pre-cooled (−80°C) GC-MS extraction solution (80:20 Methanol: Milli-Q H_2O, 1 μg/mL norvaline, 1 μg/mL adipic acid) and the extracts were dried in a speed-vac (Genevac EZ-2 Plus). The ^{13}C-labeled metabolites were detected by GC-MS. For the serum samples, 50 μl were used to extract the metabolites with the same protocol.

Primary glial cultured were generated as described previously with slight modifications (Raasch et al., 2011). For each sample, primary astrocytes, neurons and microglia were seeded in duplicates at cells density of $5x10^5$ cell density and incubated with 5 mM ^{13}C-acetate and/or 2 μM amyloid beta (Anaspac, Fremont, USA) for 6 h. respectively. Acetate concentration in the supernatant was measured using the Acetate V2 Bio kit (Roche) and recorded by a Cedex Bio Analyzer (Roche). Metabolites from $1x10^6$ ^{13}C-acetate treated cells per sample (pooled duplicates) were extracted with pre-cooled (−80°C) GCMS extraction solution (80:20

Methanol:Milli-Q H_2O, 1 μg/mL norvaline, 1 μg/mL adipic acid) and the extracts were dried in a speed-vac (Genevac EZ-2 Plus). The ^{13}C-labeled metabolites were detected using gas chromatography-mass spectrometry (GC-MS) (Agilent 5977). Correction for natural isotope abundance and calculation of fractional contribution was performed as described elsewhere (Buescher et al., 2015).

RNA-sequencing

Total RNA was extracted from FACS sorted viable $CD11b^+CD45^{low}DUMP^-$ microglia cells using The ARCTURUS *PicoPure RNA* Isolation Kit (ThermoFisher) according to manufacturer's protocol. The SMARTer Ultra Low Input RNA Kit for Sequencing v4 (Clontech Laboratories, Mountain View, CA, USA) was used to generate first strand cDNA from 500 to 750 pg total-RNA. Double stranded cDNA was amplified by LD PCR (11 cycles) and purified via magnetic bead clean-up. Library preparation was carried out as described in the Illumina Nextera XT Sample Preparation Guide (Illumina, San Diego, CA, USA). One-hundered and fifty pg of input cDNA were tagmented (tagged and fragmented) by the Nextera XT transposome. The products were purified and amplified via a limited-cycle PCR program to generate multiplexed sequencing libraries. For the PCR step 1:5 dilutions of index 1 (i7) and index 2 (i5) primers were used. The libraries were quantified using the KAPA SYBR FAST ABI Prism Library Quantification Kit (Kapa Biosystems, Woburn, MA, USA). Equimolar amounts of each library were pooled, and the pools were used for cluster generation on the cBot with the Illumina TruSeq SR Cluster Kit v3. The sequencing run was performed on a HiSeq 1000 instrument using the indexed, 50 cycles single-read (SR) protocol and the TruSeq SBS v3 Reagents according to the Illumina HiSeq 1000 System User Guide. Image analysis and base calling resulted in BCL files, which were converted into FATSQ files with the CASAVA1.8.2 software. Library preparation and RNaseq were performed at the Genomics Core Facility ''KFB - Center of Excellence for Fluorescent Bioanalytics'' (University of Regensburg, Regensburg, Germany).

Fastq files were quality controlled using FastQC (Andrews, 2019) and reads were mapped to the GRCm38 mouse genome using the Star aligner (Dobin et al., 2013). Read counts were obtained using the featureCounts program (Liao et al., 2014) in conjunction with the Gencode transcriptome version M21 (Frankish et al., 2019). Differential gene expression analysis was performed using the limma/voomWithQualityWeights pipeline in R (Law et al., 2014; Liu et al., 2015). Venn diagram was generated by using previously published tools (Heberle et al., 2015). Heatmaps were generated using the package pheatmap (Raivo, 2019). Pathway analysis was performed using Ingenuity Pathway Analysis (IPA, QIAGEN).

Gene expression analysis

FACS-sorted microglial cell populations or cultured primary microglia were collected directly in cell lysis buffer and subsequently RNA was isolated with the Arcturus Pico Pure RNA Isolation Kit (Life Technologies, Darmstadt, Germany) according to the manufacturer's protocol. Reverse transcription and real-time PCR analysis were performed using high capacity RNA-to-cDNA-Kit and Gene Expression Master Mix reagents (Applied Biosystems, Darmstadt, Germany) according to the manufacturer's recommendations. RT-PCRs were analyzed with a LightCycler 480 (Roche, Darmstadt, Germany). For gene expression analysis, we used the following TaqMan Gene Expression Assays: *β-Actin* (Mm01205647_g1), *Ddit4* (Mm00512504_g1), *Cxcl10* (Mm 99999072_m1), *Ccl5* (Mm 01302427_m1) and *Relb* (Mm 00485664_m1).

ChIP sequencing and qPCR

ChIP-sequencing was performed as described before (Datta et al., 2018). In brief, microglia were isolated as described above, however prior to antibody labeling for FACS isolation, cells were fixed in 1% formaldehyde in PBS for 10 min at room temperature, followed by incubation with 125 mM Tris buffer at pH 7.5 for 10 min at room temperature. FACS-isolated cells were resuspended in cell lysis buffer (10 mM Tris pH 8.0, 10 mM NaCl, 0.2% NP40, 1x complete protease inhibitor (Sigma Aldrich)), nuclei were pelleted through centrifugation and resuspended in nuclei lysis buffer (50 mM Tris pH 8.1, 10 mM EDTA, 1% SDS, 1x complete protease inhibitor). Chromatin was sheared using a Covaris M220 System. Further chromatin IP was using the True MicroChIP Kit (Diagenode) as per the manufacturer's protocol. Sequencing library preparation was performed using the KAPA Library Preparation Kit with Real-time PCR Library Amplification for Illumina Platforms Kit (Kapa Biosystems) as per the manufacturer's protocol. The Sequencing runs were performed on an Illumina HiSeq 2000 System as 50 bp paired end runs. Fastq files were quality controlled using FastQC and mapped to the GRCm38 mouse genome using the Star aligner. Duplicate reads were removed using Picard tools (http://broadinstitute.github.io/picard). Peak calling for replicate experiments was subsequently carried out using diffReps (Shen et al., 2013). Visualization was performed on Bigwig files generated using the DeepTools BAM Coverage script (Ramírez et al., 2014) and the Integrative Genome Viewer (IGV) (Robinson et al., 2011).

For ChIP-qPCR microglia were isolated and antibody labeled as described above. Prior chromatin IP, an aliquot of ~10% of each sample was preserved as input DNA sample. Consecutively, qPCR for *Cxcl10*, *P2ry12*, *Isg15*, *Apoe*, *Pgam*, *Pgk1*, *Echs1, Eno3*, *Actb*, *Gapdh* and *Des1* was performed to IP and input DNA samples. Percentage of histone modified DNA was calculated using input DNA values as reference.

Primers:

PGK1-f TGCCAAAATGTCGCTTTCCA
PGK1-r AGCCTTAACCTCCAAACCCA
PGAM1-f CTAAAGAGGAAGCGCGGC
PGAM1-r ATCTTTCCACTCGCTCGACA

ENO3-f GGGTGGCTTGGAGATAAATGC
ENO3-r TCCTGCACACCATGTAACCT
P2RY12-f TTACCTTGCACTGTGACCCT
P2RY12-r AGCTGCAAATTGGACTGGTG
APOE-f TGTCTTACCAGCTCCTTCCG
APOE-r ACTCCACCTCTTTCCTCTGC
ISG15-f TGAAACCCATCTGCCTCTGT
ISG15-r TCTTCACACCCACAGCTCAT
CXCL10-f CAGAAAATGACGGCAGCACT
CXCL10-r CAATGCCCTCGGTTTACAGG
GAPDH-f CTCCTGGCTTCTGTCTTTGG
GAPDH-r TGGCGTAGCAATCTCCTTTT
ACTB-f ACTGCCCCATTCAATGTCTC
ACTB-r GATGCTGACCCTCATCCACT
Des1-f TGTTCTGACCCTTACACCAGTC
Des1-r TGTGTGTGCTGACCTTTAGC

Metabolic profiling

Non-targeted and targeted metabolic profiling was performed by Daniel Stößel at Metabolic Discoveries, Potsdam, Germany as previously described with slight modifications (Stoessel et al., 2018). Microglia from two individual brains were pooled to one sample. Non-targeted Metabolite Profiling: Non-targeted Metabolite Profiling comprises analyses by LC-QTOF/MS and GC/MS. Using these methodologies metabolites can be analyzed in the range of 50 - 1700 Da with an accuracy up to 1-2 ppm and a resolution of mass/Δmass = 40.000. Metabolites measured in the LC are annotated according to their accurate mass, retention time and sum formula prediction/matching. Metabolite profiles were further explored by the bioinformatics platform. Unknown features are reported by their neutral mass and retention time (mass@RT). Targeted Metabolite analysis: The optimized method allows the unambiguous characterization and relative quantification of the requested metabolites by comparison with authentic standards. Metabolite analysis by LC–tandem mass spectrometry was performed using a LCMS-8050 by Shimadzu triple quadrupole mass spectrometer equipped with an electrospray ionization (ESI) source and operated in multiple reaction mode (MRM). Principal Component analysis (PCA) and clustering methods: PCA was calculated to illustrate the biggest variances between the different sample groups. Heatmap and fold change plot: Heatmaps are used to visualize differences between sample groups where each individual scaled value is contained in a matrix and represented by a specific value dependent color. Metabolites depicted in a Heatmap are listed by hierarchical clustering. Fold change plots visualize the degree of difference between the analyzed sample groups for each single metabolite. The degree of change is also be presented by value dependent color schemes. Statistical Significance Analysis: All normalized values of the peak intensities for all identified masses are listed in the Tables S12 and S13 including results of the significance test which was determined by using a unpaired Welsch‘s t test with a p value $\leq$ 0.01 after p value correction by using false discovery rate adjustment (Benjamini and Hochberg, 1995).

Oxaloacetic acid measurement

Oxaloacetic acid assay was performed using Oxaloacetate Assay Kit (Abcam, ab83428) following the manufacturer’s recommendations. FACS-isolated microglia were pooled from 5 individual mice to obtain $\sim$1,4 million cells per sample. Prior the assay samples were deproteinized using Deproteinizing Sample Preparation Kit - TCA (Abcam, ab204708).

Proteomics

Four replicates of isolated microglia from SPF mice were compared to five replicates of isolated microglia of GF mice in a labelfree proteome comparison. Each replicate consisted of 800000 microglia isolated from four mice (200000 cells / mouse). The pooled microglia were lysed in 0.1% RapiGest (Waters, Milford, MA), 0.1 M HEPES pH 8.0 (AppliChem, Darmstadt, Germany) and protease inhibitors: 10 μM trans-epoxysuccinyl-l-leucylamido (4-guanidino)butane (E-64), 10 μM E64d, 10 mM phenylmethanesulfonyl fluoride (PMSF), 5 mM ethylenediaminetetraacetic acid (EDTA). Briefly, samples were sonicated using a Bioruptor device (Diagenode, Liège, Belgium), proteins were reduced using 5 mM dithiothreitol (DTT) (AppliChem, Darmstadt, Germany), alkylated using 15 mM 2-iodoacetamide and digested using sequencing grade trypsin (Worthington, 1:25 enzyme:protein ratio). After removal of RapiGest, samples were desalted by C18 solid phase extraction (HyperSep, Thermo). One ug of peptides were analyzed on a Q-Exactive Plus mass spectrometer (Thermo Scientific, San Jose, CA) coupled to an EASY-nLCTM 1000 UHPLC system (Thermo Scientific). The analytical column was self-packed with silica beads coated with C18 (Reprosil Pur C18-AQ, d = 3 Â) (Dr. Maisch HPLC GmbH, Ammerbusch, Germany). For peptide separation, a linear gradient of increasing buffer B (0.1% formic acid in 80% acetonitrile, Fluka) was applied, ranging from 5 to 40% buffer B over the first 90 min and from 40 to 100% buffer B in the subsequent 30 min (120 min separating gradient length). Peptides were analyzed in data dependent acquisition mode (DDA). Survey scans were performed at 70,000 resolution, an AGC target of 3e6 and a maximum injection time of 50 ms followed by targeting the top 10 precursor ions for fragmentation scans at 17,500 resolution with 1.6 m/z isolation windows, an NCE of 30 and an dynamic exclusion time of 35 s. For all MS2 scans the intensity threshold

was set to 1.3e5, the AGC to 1e4 and the maximum injection time to 80 ms. Data were analyzed with MaxQuant (v 1.6.14.0) allowing two missed cleavage sites, no variable modifications, carbamidomethylation of cysteines as fixed modification, using label free quantification (LFQ), and match between runs (MBR) set to activated. The Mouse-EBI-reference database was downloaded from https://www.ebi.ac.uk/ on Feb 4th 2020. Only unique peptides were used for quantification. Data were normalized with MSstats.

Electron microscopy

Following standard EM protocols, samples were first fixed overnight in 3% glutaraldehyde at 4°C, washed with Sörensen buffer and then transferred to 1% osmium tetroxide for 2 h. at room temperature. After washing samples with aqua bidest, they were dehydrated by a graded series of ethanol (30%–100%) followed by 100% propylene oxide (PO), resin/PO [1:2 (v/v)], and resin/PO [2:1 (v/v)]. Samples were embedded in resin via polymerization for 24 h at 75°C. 700 nm semi-thin sections were cut and stained with 2% toluidine blue to define the region of interest for further preparation of 70 nm ultra-thin sections using an ultramicrotome (Leica Reichert Ultrachut S). After contrasting the sections with uranyl acetate and lead citrate (Leica Reichert Ultrostainer) following standard protocols, images for were taken at 7900 × or 46000x magnifications using CM100 Electron Microscope (Philips). Images were analyzed using Photoshop (Adobe) and iTEM Software (Olympus). For immunogold labeling of Iba1 and PU.1 samples were fixed in 0.1% glutaraldehyde and 4% PFA (in phosphate buffer, 0.1 M) for at least 3 h. 50 μm sections were prepared using a Leica VT1000S vibratome and sections were consecutively incubated with rabbit anti-Iba1 (1:50) or rabbit anti-PU.1 (1:50) in 2% NGS (v/v) containing TBS (Tris-buffered saline; 50 mM)) at 4°C overnight. Sections were washed for 1 h in TBS (50 mM) and incubated with secondary goat anti-rabbit antibodies (Nanoprobes, #2004; 1.4 nM gold coupled, 1:100 dilution in 2% NGS (v/v) containing TBS (50 mM)) at 4°C overnight. After washing for 30 min in TBS (50 mM), sections were postfixed in 1% (w/v) glutaraldehyde containing PBS (25 mM) for 10 min. Sections were washed again and a silver intensification (HQ Silver Enhancement Kit, Nanoprobes, #2012) was performed according to the manufacturer's instruction. Slices were incubated with 0.5% osmium tetroxide for 40 min, washed in graded ethanol (up to 60% (v/v)) for 10 min each and incubated with uranylacetate (1% (w/v) in 70% (v/v) ethanol) for 35 min. Slices were then dehydrated in graded ethanol (80%, 90%, 95%, 2x 100% for 10 min). Two washing steps in propylenoxide for 5 min each were performed before incubation with durcupan/propylenoxide (1:1 for 1 h) and consecutive transfer to durcupan overnight at room temperature. Slices were embedded in durcupan and ultrathin sectioning (60 nm) was performed using a Leica UC6 Ultracut. Images were taken with a TEM LEO 906 (Zeiss) equipped with a Sharp-Exe 2k camera and processed with Image SP (Tröndle, Germany). Up to 50 cells per individual mouse were analyzed.

Western blot

Adult microglia were isolated from the entire brain by performing fluorescent-activated cell sorting (FACS). Total protein from 200.000 FACS-sorted cells were extracted in RIPA buffer (25 mM Tris-HCl, 150 mM NaCl, 1% Nonidet P-40, 0.5% sodium deoxycholate, 0.1% SDS, pH 7.5). Samples were separated by using Novex system. Immunoblots were blocked in 5% milk in 1xTBST for 1 h at room temperature, followed by incubation with primary antibodies directed against SDHA and VDAC (1:1000 in 2.5% BSA in 1xTBST, Cell Signaling) overnight at 4°C. Blots were washed 3x in 1xTBST and subsequently incubated with HRP-linked secondary antibody for 1 h at RT (1:2000, Cell Signaling). HRP-linked β-ACTIN (1:5000, Abcam) was used as loading control. SuperSignal West Femto Maximum Sensitivity Substrate ECL (ThermoFisher) was used for protein detection and immunoblots were imaged in a Gel Imaging Systems ChemiDoc XRS (Bio-Rad).

QUANTIFICATION AND STATISTICAL ANALYSIS

Statistical analysis

Statistical analysis was performed using GraphPad Prism (GraphPad Software, Version 5.0, La Jolla, USA). All data were tested for normality applying the Shapiro-Wilk normality test. If normality was given, an unpaired t test, one-way ANOVA followed by Tukey's post hoc comparison test or two-way ANOVA followed by Tukey's post hoc comparison test was applied respectively. Differences were considered significant when p value < 0.05 and marked with asterisks (*$p < 0.05$, **$p < 0.01$, ***$p < 0.001$). Each symbol represents one mouse. Means ± SEM are shown. To obtain unbiased data, experimental mice were all processed together and cell quantifications were performed blinded by two scientists independently and separately.